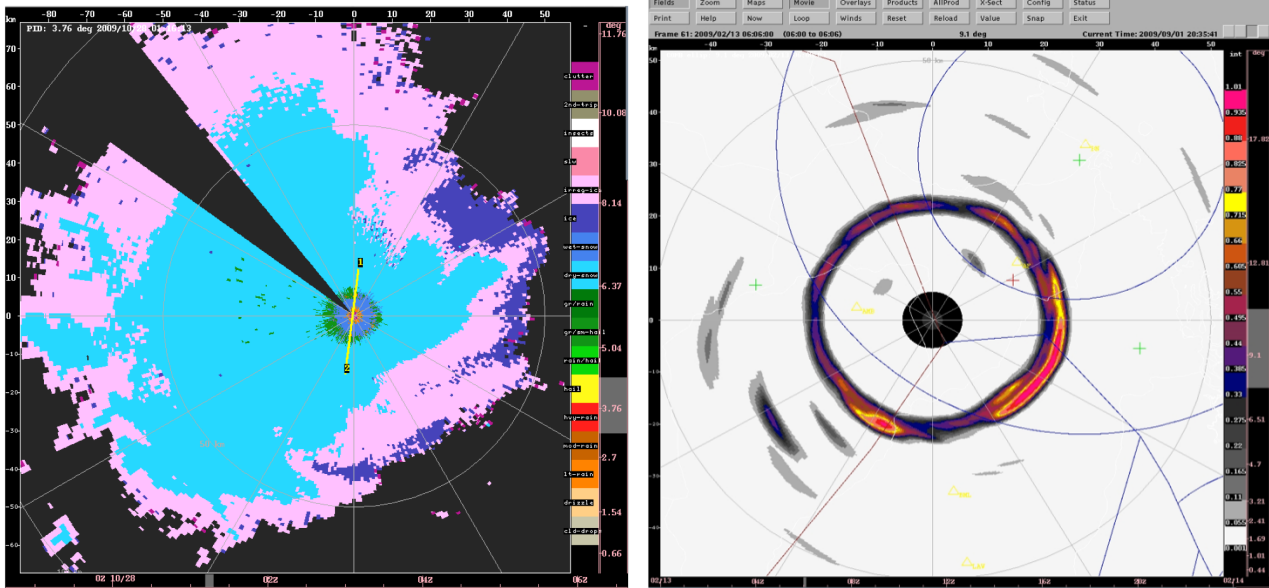# Icing Hazard Level Detection

Final Report

Derived radar data fields: Left, PID data. Right, Ring Filter data

Prepared for: MIT Lincoln Laboratories

By: David Albo, Scott Ellis, Mike Dixon, Andrew Weekley, Marcia Politovich, Gary Cunning and John C. Hubbert
Scientific Lead: John C. Hubbert

National Center for Atmospheric Research
Research Applications Laboratory

30 June 2010

NCAR

Contents

Eecutive Summary

This is the Final Report of the Icing Hazard Level (IHL) activities performed by NCAR for MIT Lincoln Laboratory. The task is to develop an Icing Hazard Level Algorithm (IHLA) that utilizes dual-polarization radar data and the temperature (T) and relative humidity (RH) fields from the RUC (Rapid Update Cycle) model. This work has been motivated the upcoming dual-polarization of the NEXRAD network. The starting point of this effort was informed by existing algorithms:

1. freezing level detection;

2. freezing drizzle detection;

3. Hydrometeor Classification Algorithm (HCA) and Particle Identification (PID)algorithm;

4. and general knowledge base at NCAR acquired from the development of the CIP (Current Icing Product; Berstein et al. (2005)) algorithm.

This knowledge base is used to fashion an initial IHLA. Experimental data sets from CP2, S-Pol and CSU-CHILL are used to test and illustrate some of the subcomponents of the proposed IHL algorithm. Though far from an operational algorithm, this preliminary design shows promise. More dual-polarization data sets of icing condition environments need to be collected. Such data will be vital to creating, refining and tuning a more robust and verifiable IHLA.

1 Introduction

The initial IHLA reported here is based on existing principles, knowledge and several prior developed algorithms. Here we give a brief description of this foundation. The existing algorithms and knowledge used are freezing (melting) layer detection, freezing drizzle detection and hydrometeor classification algorithms.

Identification of supercooled liquid water using dual polarimetric radar has been investigated before by researchers who developed the PID (Particle Identification) fuzzy logic algorithm (Vivekanandan et al. 1999). They found that the polarimetric membership functions for supercooled liquid water completely overlapped with irregular-shaped ice, i.e., ice that is characterized by zero average Z_{dr} (differential reflectivity) and zero average K_{dp} (specific differential phase). The fuzzy logic used by PID, however, to distinguish these particle classes is base on the radar variables at one gate or resolution volume. Recently, Ikeda et al. (2009) have developed a freezing drizzle detection algorithm for the WSR-88D radars that is based in large part on various metrics of spatial texture of reflectivity. They found that drizzle exhibited smoother reflectivity textures than ice particles and thus they were able to discriminate between these two particle classes at least for 70% of their observed drizzle cases. Plummer et al. (2010) have recently made similar type observations from comparisons of aircraft observations (particle probes) and S-Pol data from the field campaign MAP in northern Italy. They examined histograms of Z_{dr} and K_{dp} and concluded that 1) the mean values of K_{dp} and Z_{dr} were greater in regions of ice-only as compared to mixed-phase and 2) the texture of Z_{dr} and K_{dp} were also greater in regions of ice-only as compared to mixed-phase. Thus, these new studies indicate that radar data, and in particular dual-polarization radar data, can offer skill in identifying aircraft icing conditions.

2 Freezing Level Detection

There are several existing techniques for estimating freezing level of hydrometeors, for example Brandes and Ikeda (2004). This algorithm, however, uses vertical profiles of radar data. Since WSR-88D only gathers PPI data, it is desirable to identify the freezing level directly from PPI data rather than reconstructed vertical cuts. Later we describe a freezing level detection technique developed at NCAR for this project that utilizes PPI data.

As ice particles descend through the $0°C$ isotherm, they begin to melt, can aggregate, and finally turn into liquid drops. This process typically produces enhances radar signatures and distinct vertical profiles of radar data. The vertical profiles of radar parameters of the melting layer are shown in Fig. 1 (borrowed from Brandes and Ikeda (2004)). Melting level detection routines capitalize on this information.

3 Freezing Drizzle (FZDZ) Detection

The central principle in detecting FZDZ in Ikeda et al. (2009) is that mixed-phase precipitation and snow (ice crystals) produce higher spatial variability of reflectivity signatures than drizzle. This spatial variability is cause by 1) vertical gradients in reflectivity and 2) the presence of larger variable-sized ice particles (compared to drizzle). The vertical gradient in reflectivity (Z) is cause by the onset of the formation of
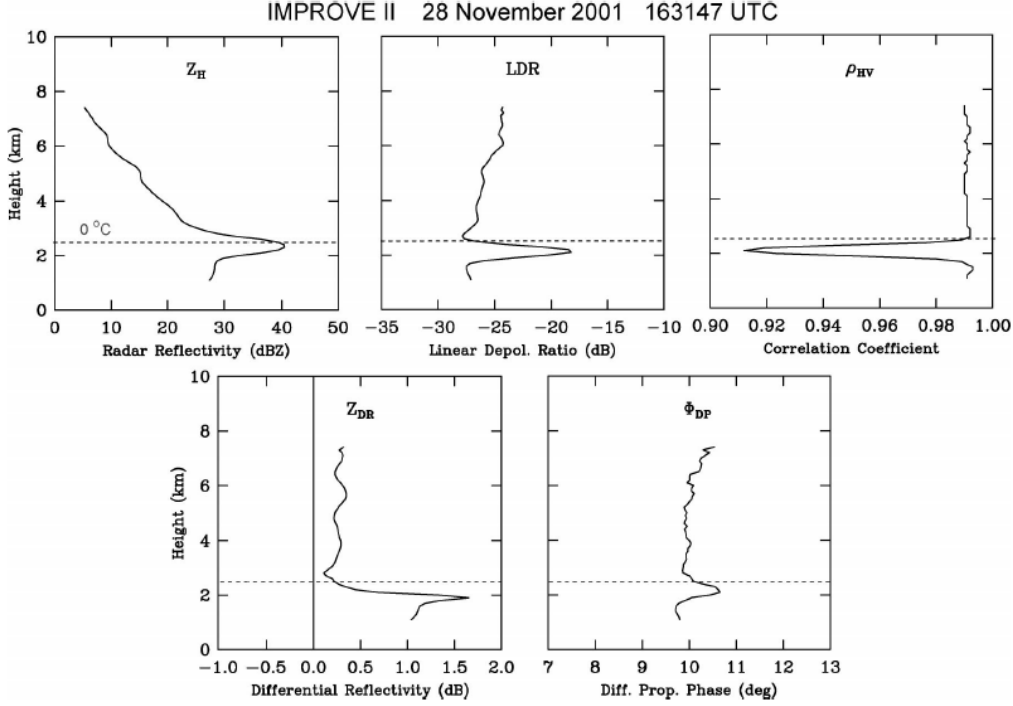
FIG. 1. Profiles of polarimetric measurements (Z_H, LDR, ρ_{HV}, Z_{DR}, and Φ_{DP}). The estimated 0°C level (2.47 km) is shown by a horizontal line. Heights are above mean sea level.

Figure 1: *Vertical polarimetric radar profiles of the melting level (from Brandes and Ikeda (2004)).*

ice (snow) which creates larger particles than found in pure drizzle (Fabry and Zawadski 1995). Colder (cooling of) cloud tops likely drives the ice nucleation process. The larger particle cause both larger Z (due to D^6) and greater Z variance (speckle). The vertical gradient will also increase texture estimates such as the standard deviation of Z. Texture estimates, such as the one used in Ikeda et al. (2009)

$$Z_T = \frac{\sum\limits_{j=1}^{m} \sum\limits_{i=1}^{n} (Z_{i,j} - Z_{i-1,j})^2}{n \times m - 1},$$ (1)

are less influenced by the vertical gradient increase as compared to the standard deviation. The vertical gradient noted in Ikeda et al. (2009) is below 2.5 km MSL or about 0.9 km AGL in the Front Range. The standard deviation is defined in usual fashion as

$$\sigma_{z,local} = \sqrt{\frac{\sum\limits_{j=1}^{m} \sum\limits_{i=1}^{n} (Z_{i,j} - \bar{Z})^2}{n \times m - 1}}$$ (2)

where $\bar{Z}$ is the mean reflectivity. m and n define the grid over which the Z_T and $\sigma_{z,local}$ are calculated.

Ikeda et al. (2009) divide the area around the radar into two regions: $R_1 : r \leq 15$ km; $R_2 : r \leq$ 100 km. The elevation angle versus range is used as a vertical profile proxy for the 100-km region.

5

In short, drizzle is characterized by:

1. weak median reflectivity (0-5 dBz)

2. spatially-uniform reflectivity field

3. relatively small vertical gradient of reflectivity compared to mixed-phase/snow

4. small vertical extent (less than a few kilometers)

The radar parameters used in Ikeda et al. (2009) are

1. median radar reflectivity over entire 15 km and 100 km domains (Z_m dBZ)

2. global standard deviation of reflectivity over entire 15 km and 100 km domains ($\sigma_{z,global}$ dBZ)

3. median local standard deviation (median $\sigma_{z,local}$ dBZ).

4. standard variation of the local standard deviation (standard deviation of $\sigma_{z,local}$) dBZ

5. median reflectivity texture within circular areas of 15- and 100-km radii centered at the radar site (median Z_T).

The membership functions are given in Fig. 2 (from Ikeda et al. (2009)). Thus, the algorithm calculates numerous statistical measures and uses fuzzy logic to convert these measures into scores; the individual scores are then combined into a single final score. If the final score is above a threshold, freezing drizzle is inferred to be present in the scan. While this algorithm will not suffice for aircraft icing detection, it does provide a reasonable starting point.

4 Plummer: Aircraft Data Compared to Radar Observations

Plummer et al. (2010) report polarimetric signatures of mixed-phase and ice-only regions of storms from the field campaign MAP in the Italian Alps (1999). Measurements of particle probes mounted onto the ELECTRA research aircraft are compared to S-Pol data. The frequency histograms shown in Fig. 3 are for mixed-phased (left column) and ice-only (IO; right column) regions. Mixed-phase areas are considered indicative of SLW (supercooled liquid water).

Of particular interest are the histograms of Z_{dr} (c),(d) and K_{dp} (e),(f). The histograms for the mixed-phase region are narrower than the histograms for the ice-only region. This suggests that such histograms from experimental radar data could discriminate the two classes. They also suggest that spatial texture of Z_{dr} and K_{dp} will be higher in ice-only regions as compared to mixed-phase regions. Possible texture estimates are 1) mean reflectivity difference (e.g., Eq.(1)), 2) standard deviation and 3) the standard deviation of (1) and (2).
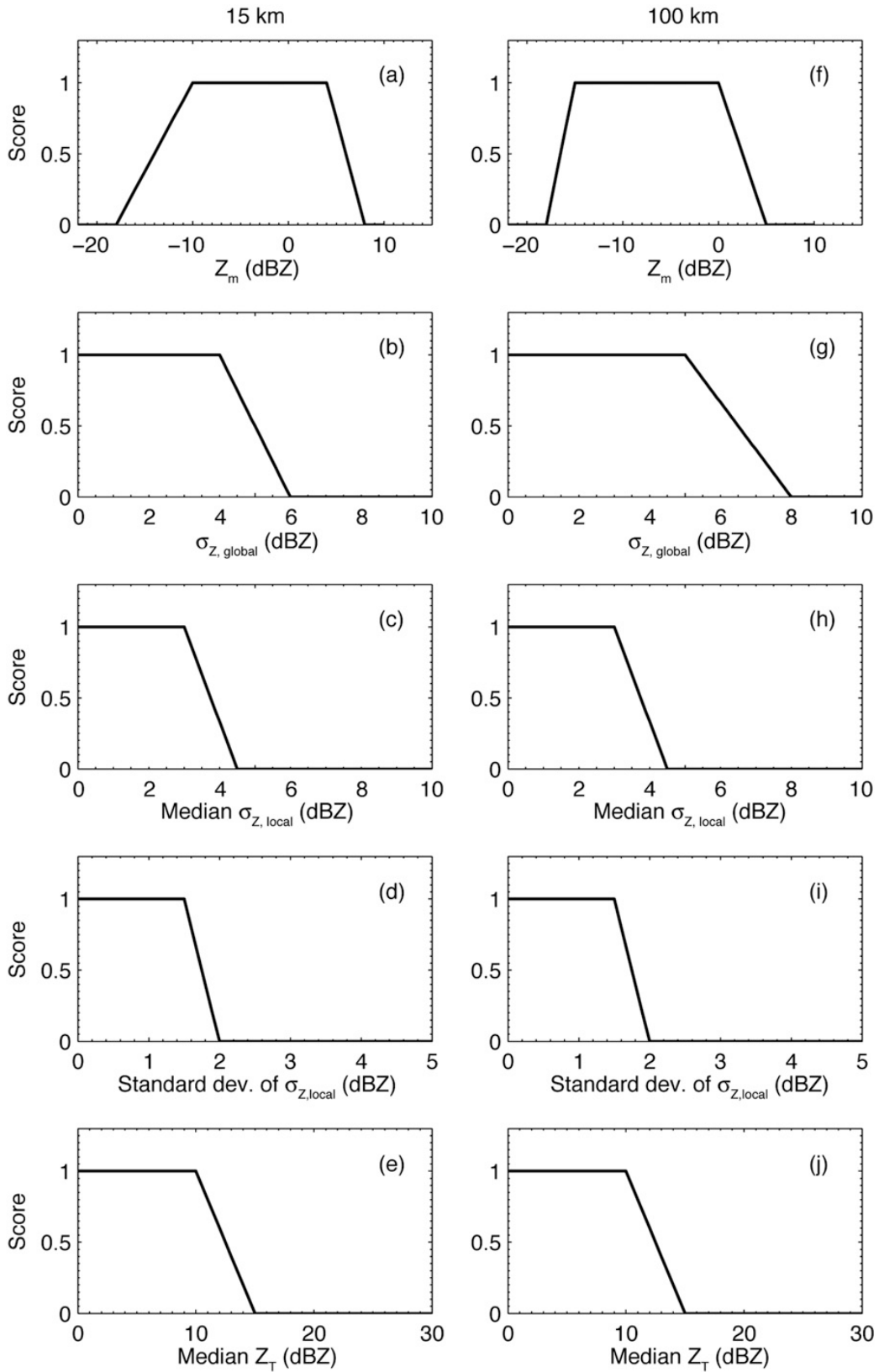
Figure 2: *Membership functions for radar echo feature parameters corresponding to areas inside the (a)(e) 15-km and (f)(j) 100-km range marks. (from Ikeda et al., 2009).*

5 An Algorithm to Find Freezing Level from Dual-Polarized Radar Data

a *Introduction*

As discussed and shown above, when hydrometeors transition from frozen or solid particles to a liquid state, vertical profiles of radar variables typically display distinct features. Using these features, a freezing level detection algorithm was designed that uses PPI data. When viewing PPI scans of radar data (rather than vertical cuts or RHI data) the freezing level is typically seen as a "ring" of values that are different than the values above or below (nearer and farther) the freezing level range. The following algorithm finds these rings on a PPI-to-PPI basis, and from them estimates a freezing level as a height Z above the radar.

b *Ring Filter*

The human eye can easily see a ring of distinct values in the following ρ_{hv} images shown in Fig. 4. Each image represents a PPI scan of the radar at a different elevation angle. These rings mark the freezing level and typically occur at a constant height above the radar at least for typical stratiform-type precipitation. The ring, therefore, is seen closer to the image center and becomes less deep as the elevation angle increases. The ring filter algorithm attempts to identify the ring-like pattern in the same way that the eye does. This is done using a moving two-dimensional spatial template that defines a set of points over which to perform a calculation. The set of points is defined by the template, and it changes based on the center-point of the template. The template consists of three regions: center, inner and outer. The data values in each of these regions are used to compute a "ring interest" in the range 0 to 1 with 1 being extremely ring-like and 0 being not at all ring-like. The diagram in Fig. 5 shows an example of the ring template centered at a particular point (r,a) with r and a denoting range and azimuth respectively.

The data difference between the center (green) region and the non-center (blue and red) regions are computed, and a derived value Ring(r,a) is computed for that point. For the previous ρ_{hv} images in Fig. 4, the ring filter yields the interest images shown in Fig. 6. The template that was used is shown in the images at top right of center (pink and brown curved bars).

The actual rings seen in the previous ρ_{hv} images of Fig. 4 can be seen in the filtered images marked by high interest values while other points are typically significantly lower. However, some areas manifest a local ring-like feature even though they are not part of the actual ring.

Because the ring finding algorithm leads to spurious local false high values which tend to be non-contiguous whereas the actual ring high values are more contiguous, as seen above, a second ring filter is applied to the first filtered images, to bring out contiguous rings. The resulting double filtered ρ_{hv} images are shown in Fig. 7. It can be seen that the second filter preserved the high values where appropriate, whereas in other areas, the values tended to be decreased.

i Ring Filter Example for Reflectivity The same approach can be used on other radar fields that potentially show the ring-like patterns. Only the templates and parameters change. Shown in Fig. 8 is PPI dBZ (denoting reflectivity) data corresponding to the 9.1° elevation angle ρ_{hv} data of Fig. 4. The left hand image is dBZ while the right hand image is the dBZ data processed by the ring filter.

ii Ring Filter Example for Z_{dr} In a similar fashion, Z_{dr} PPI data corresponding to the above ρ_{hv} and dBZ data is processed by the ring filter. Figures 10 and 11 similarly show Z_{dr}, Z_{dr} processed by the ring filter (in Fig. 10) and Z_{dr} processed twice by the ring filter (Fig. 11).

iii Combining the Ring Filter Results When the fields of ρ_{hv}, dBZ and Z_{dr} are processed from the same radar scan with the double ring filter, skill is seen, but gaps do show up, with different gaps and weaknesses depending on the input data field. For the 9.1° scan example, the ρ_{hv}, dBZ and Z_{dr} double ring filter data from Figs. 7, 9, and 11, respectively, are combined. The combine filter selects the maximum at each grid-point from a set of inputs to fill in the fields. The result of combining these three fields is shown in Fig. 12. As can be seen, the ring feature that marks the region of the freezing layer is identified without gaps that were apparent in the individual ρ_{hv}, dBZ and Z_{dr} images. In the maximum filtered image of Fig. 12, there is a small area to the lower left that has high interest. Applying an average filter can reduce smaller areas of high interest, and retain larger areas of high interest, depending on the filter size. We next apply a simple averaging filter to reduce small isolated high-interest areas and this is shown in Fig. 13.

c *Clumping Filter*

Within the image of Fig. 13, the eye easily picks out a contiguous region with high interest, and in this case forms an almost perfect circular ring. A clumping algorithm builds contiguous clumps above a threshold, and each resultant clump is evaluated for quality. Quality is a fuzzy measure based on various size, shape and data value factors.

The result of clumping of the example is shown in Fig. 14 with each clump displayed with its quality value (0 to 1). Two clumps with quality in the upper 0.6's, and a small clump with lower quality (0.5) are seen. Note that both big clumps are at a similar radius (freezing level).
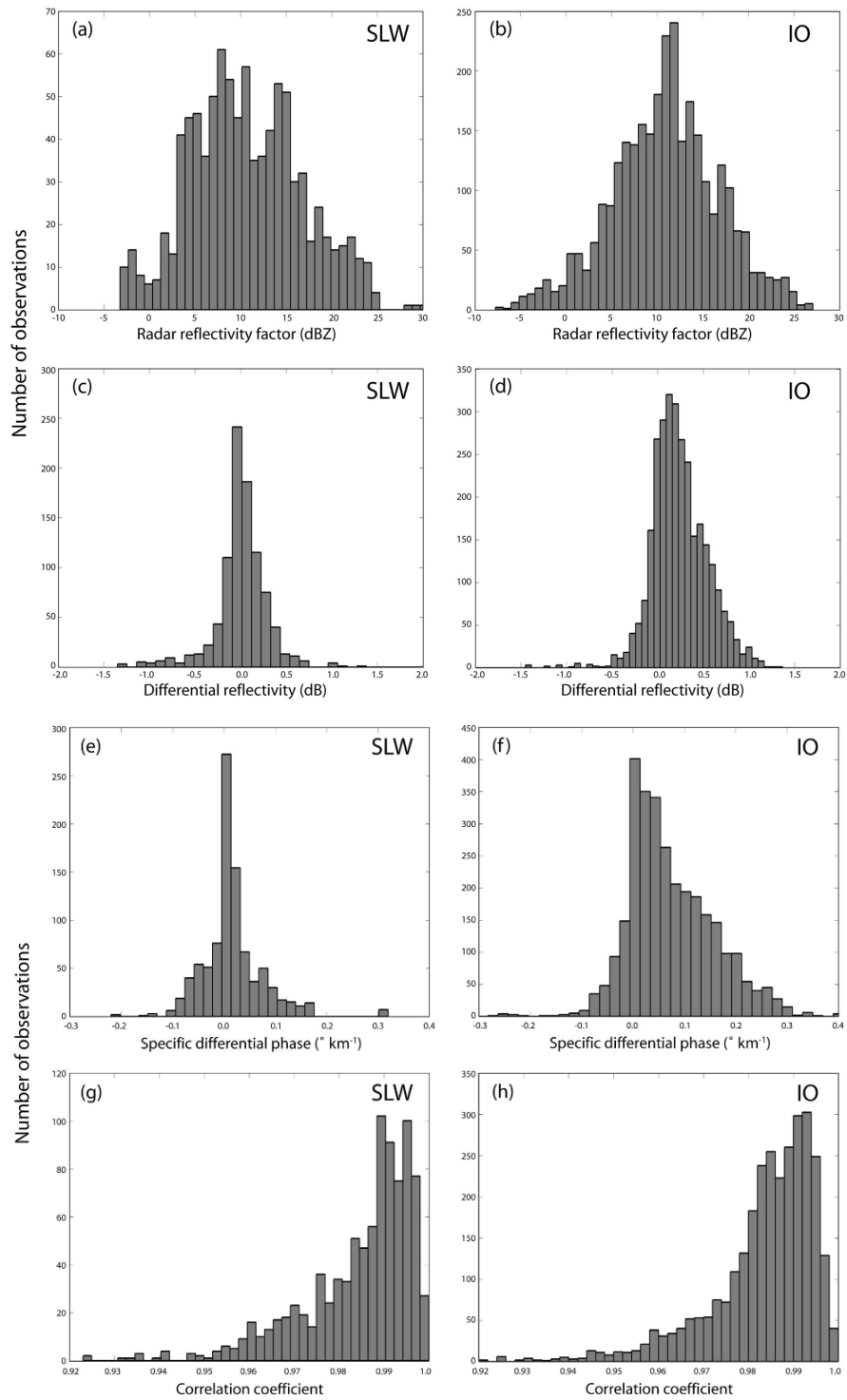
9

Figure 3: *Frequency histograms of observed values of radar reflectivity factor (dBZ) for (a) SLW and (b) IO (ice-only); differential reflectivity (dB) for (c) SLW and (d) IO; specific differential phase ($°km^{-1}$) for (e) SLW and (f) IO; correlation coefficient for (g) SLW and (h) IO (from Plummer et al., 2010).*
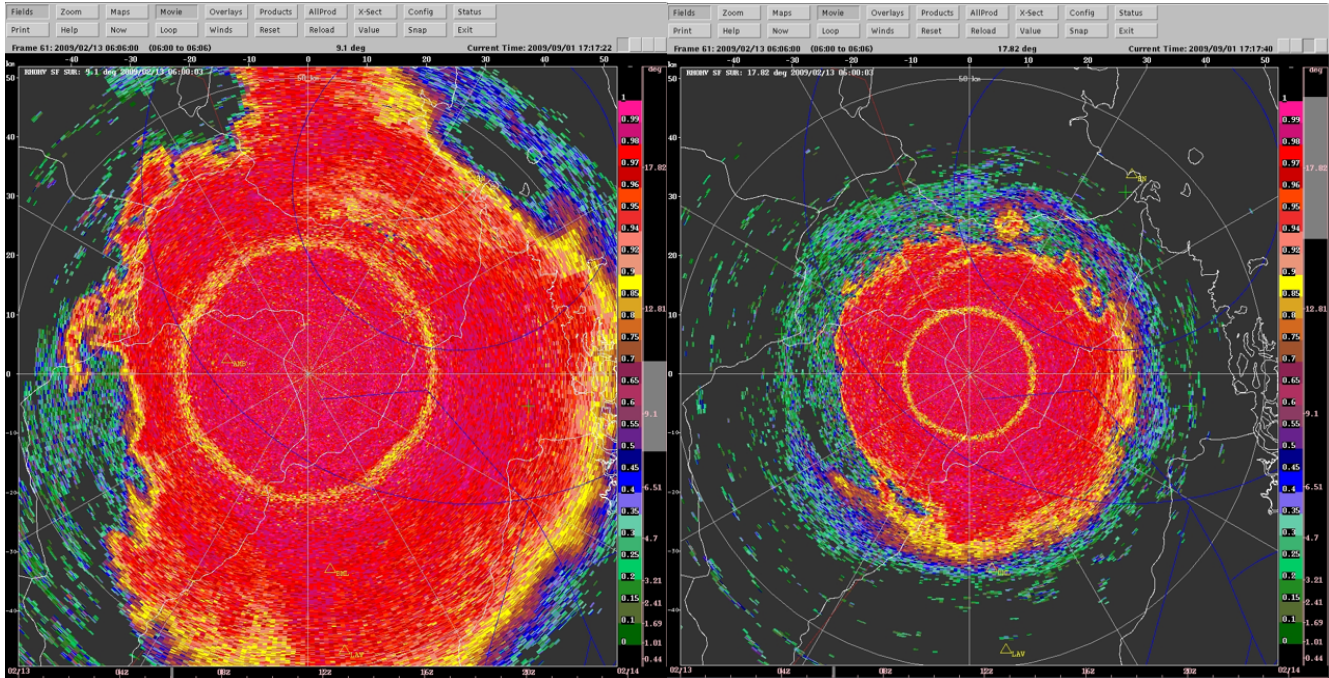
Figure 4: *PPI ρ_{hv} data from the CP2 radar located in Brisbane, Australia, operated by the The Centre for Australian Weather and Climate Research. Left: 9.1° elevation. Right: 17.8° elevation*
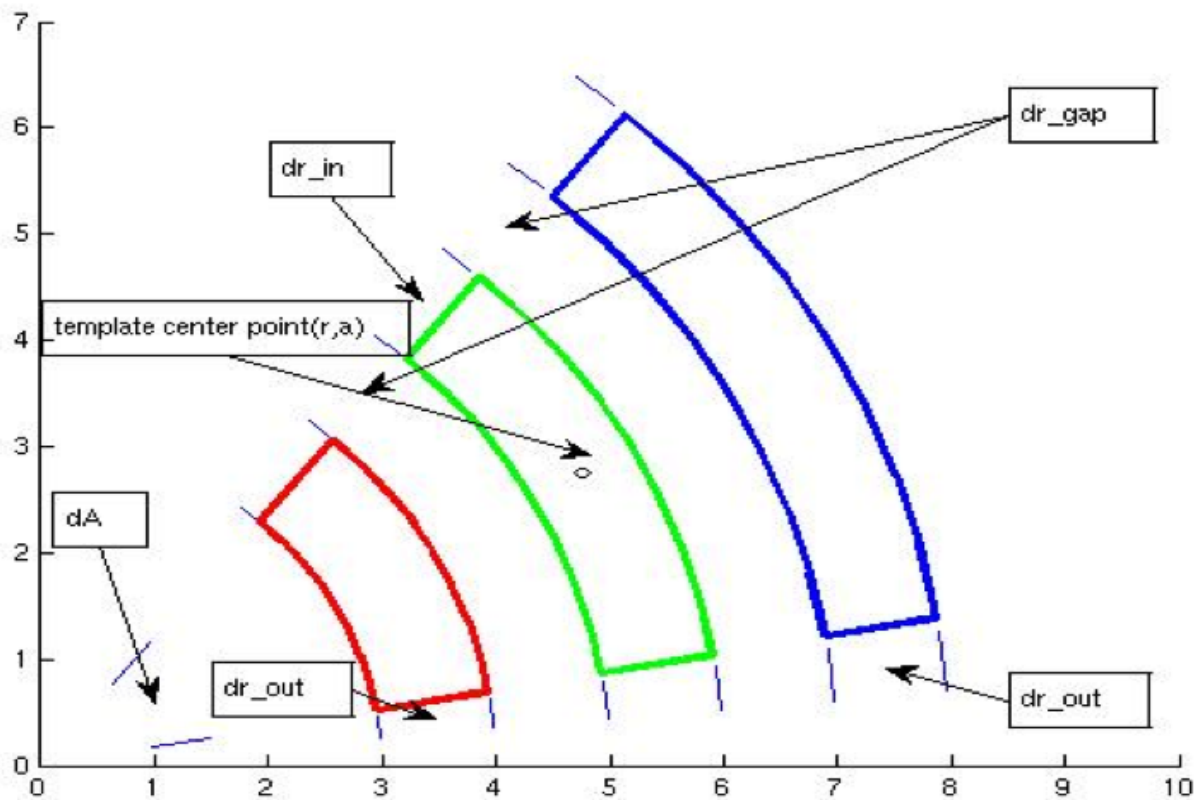
Figure 5: *A diagram illustrating the ring filter used to detect the freezing level.*
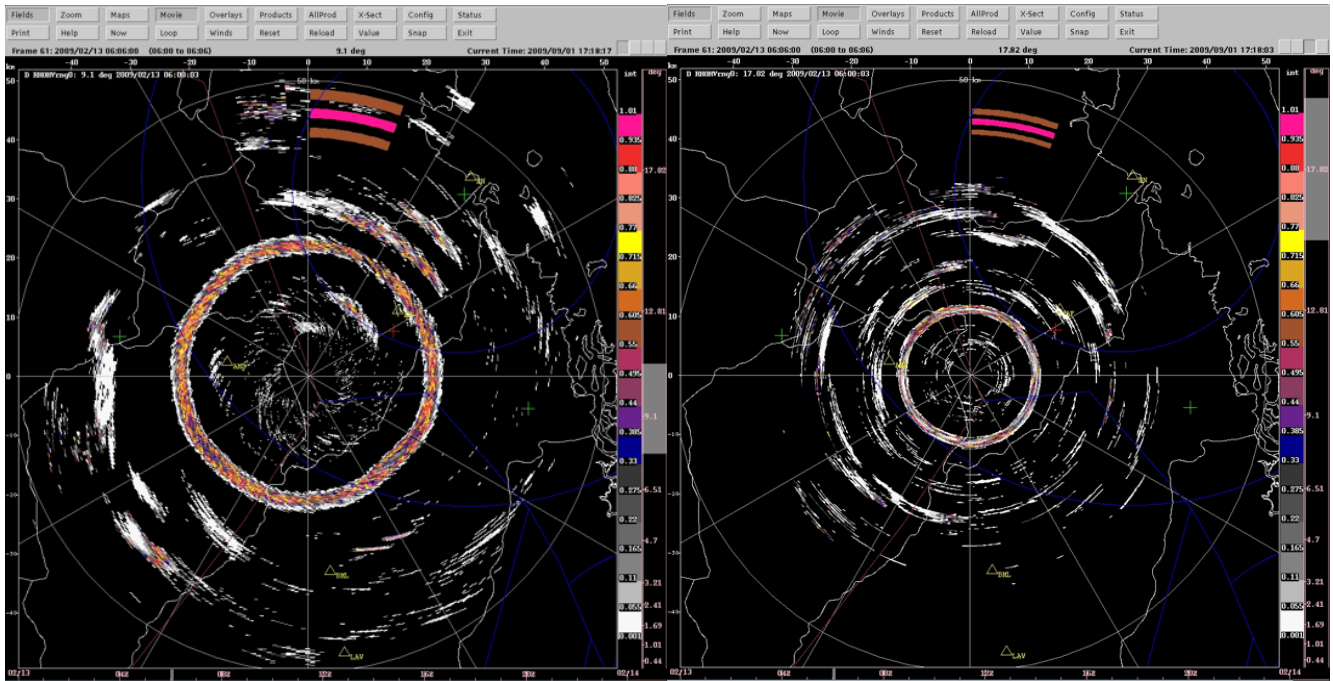
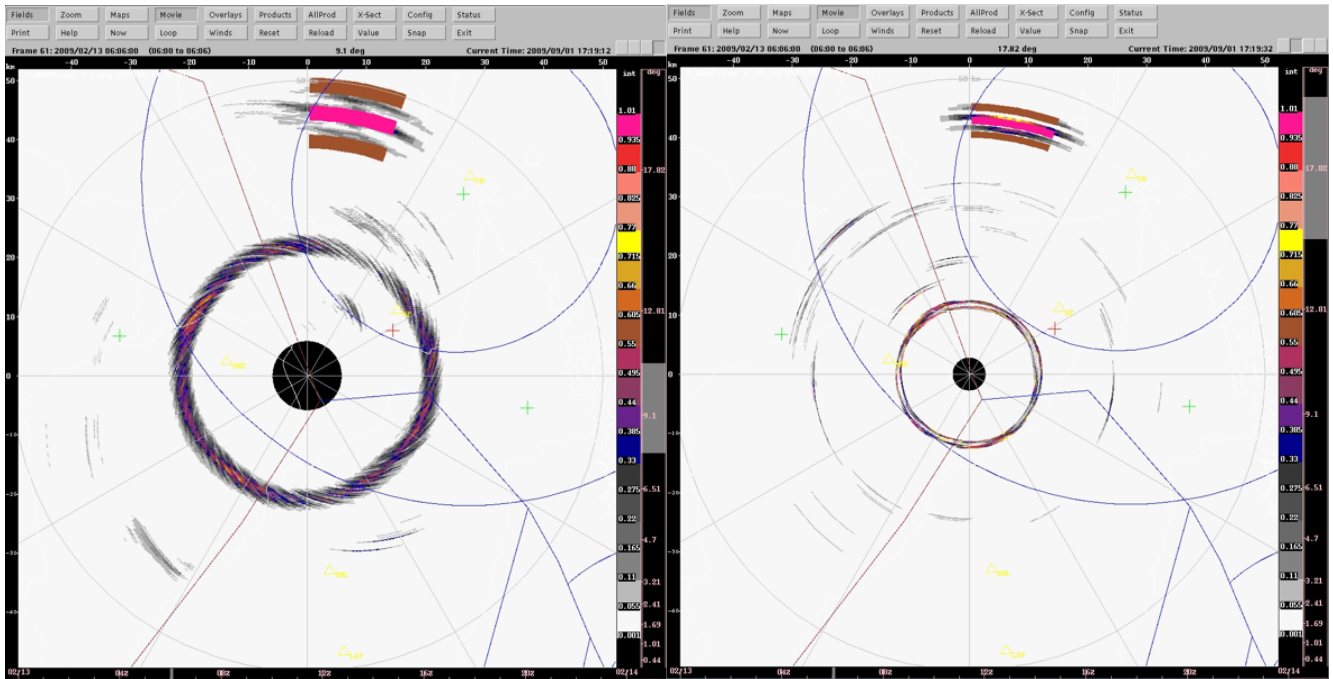Figure 6: *PPI ρ_{hv} data from Fig. 4 that has been processd by the ring filter.*

Figure 7: *PPI ρ_{hv} data from Fig. 6 that has been processed by the ring filter a second time.*
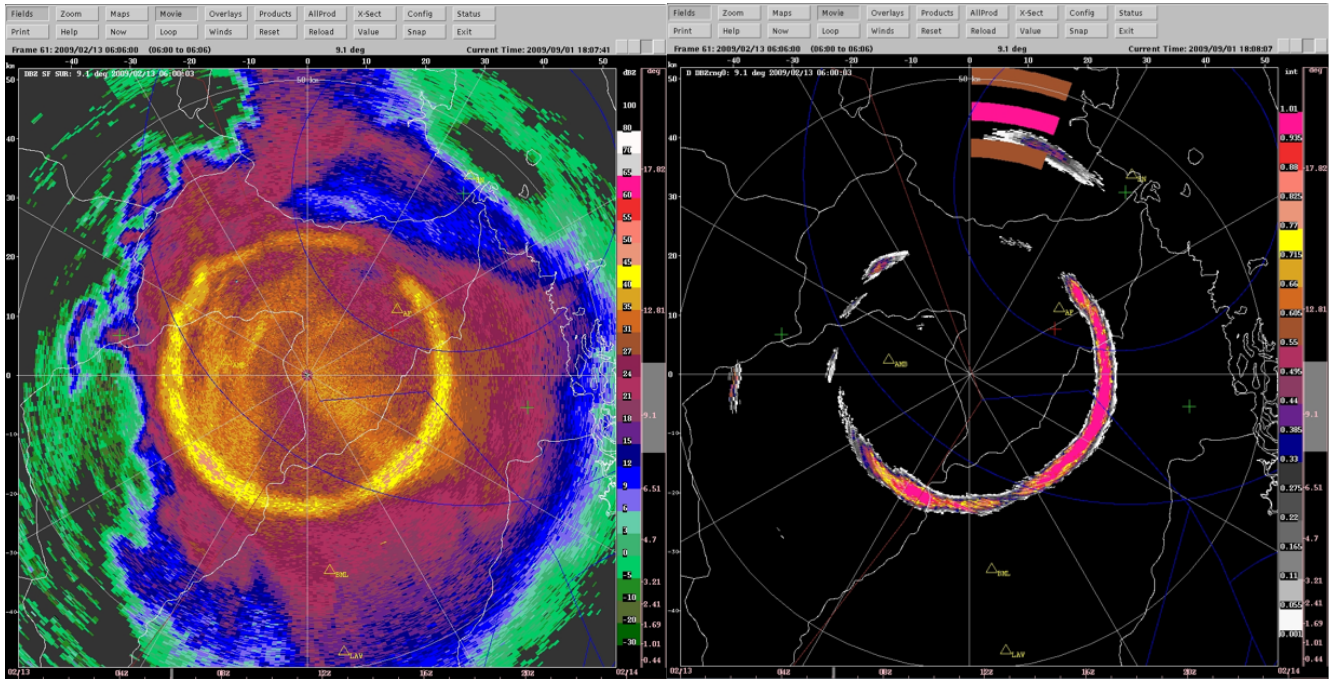
Figure 8: *PPI dBZ data corresponding to Fig. 4. The left image is dBZ and the right image is the dBZ data processed by the ring filter.*
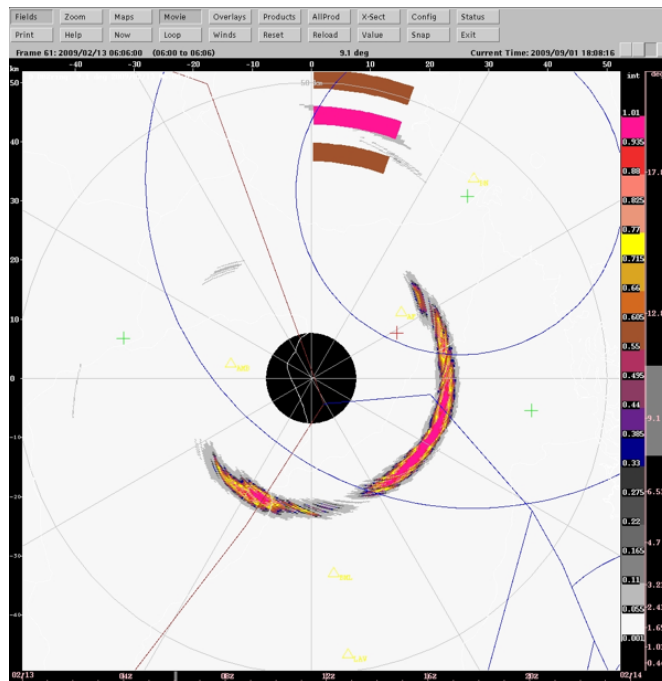

Figure 9: *PPI dBZ data corresponding to Fig. 8. The image is the dBZ data processed twice by the ring filter.*
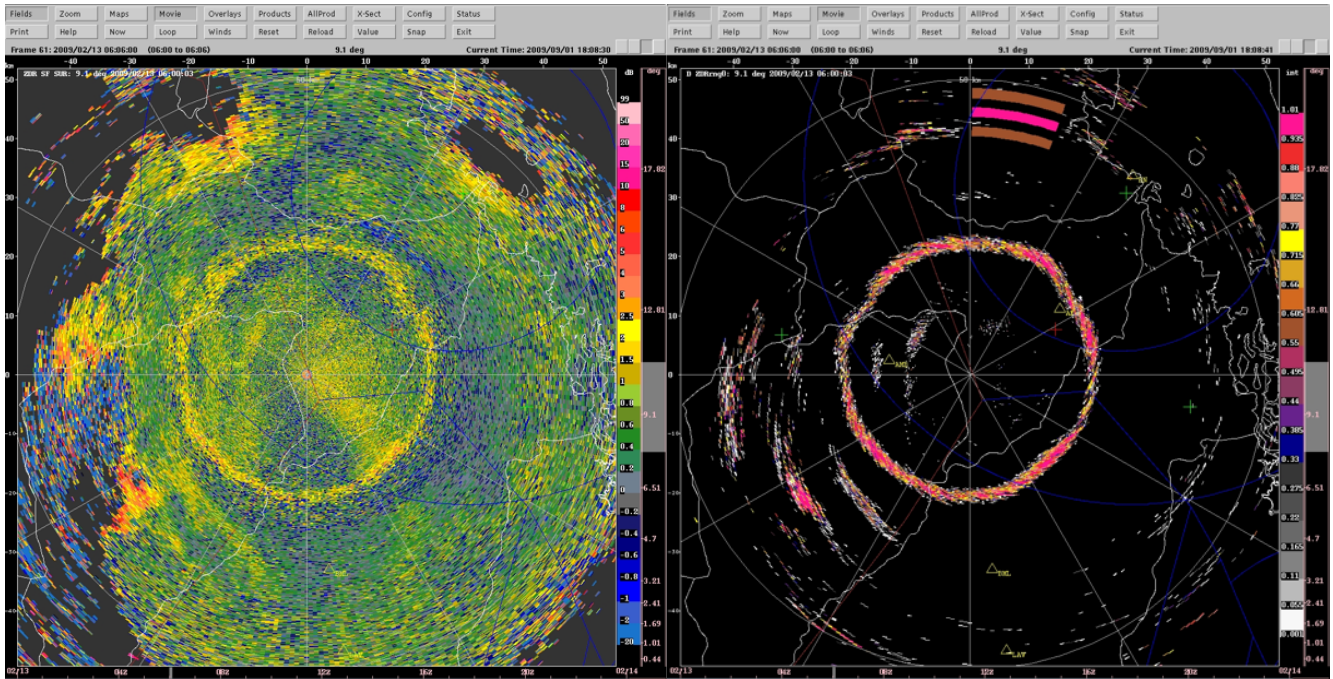
Figure 10: *PPI dBZ data corresponding to Fig. 8. The left image is Z_{dr} and the right image is the Z_{dr} data processed by the ring filter.*
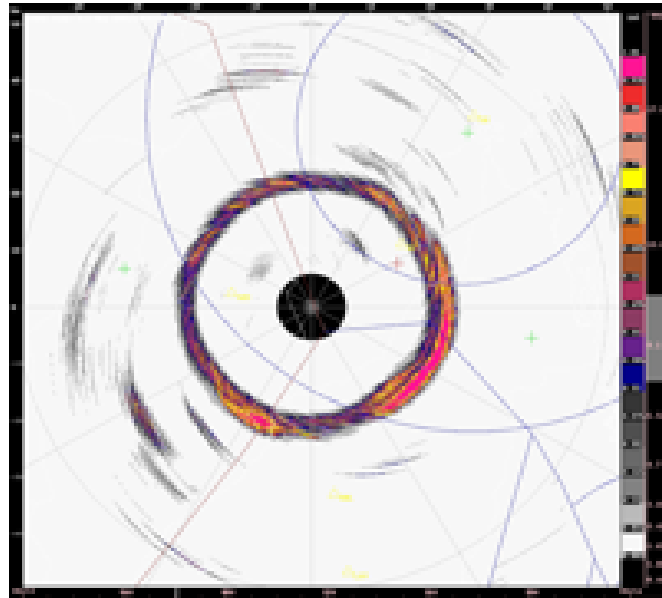

Figure 11: *PPI Z_{dr} data corresponding to Fig. 8. The image is the Z_{dr} data processed twice by the ring filter.*
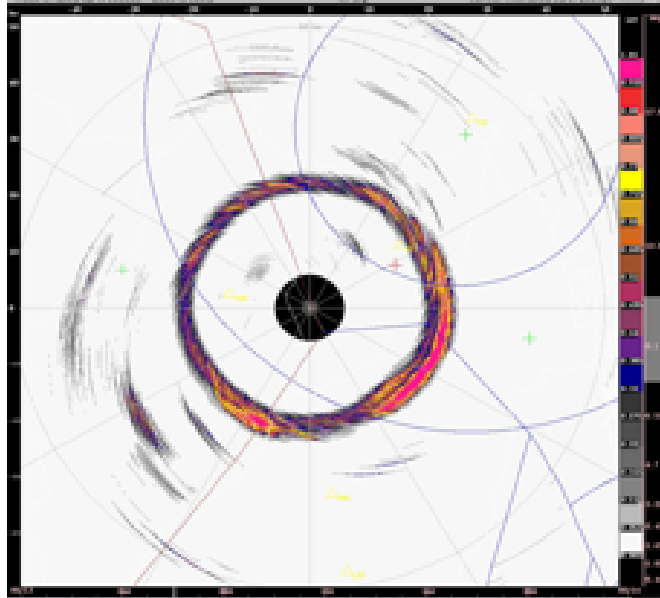
Figure 12: *PPI ring feature data generated from a combination of the double ring filtered ρ_{hv}, dBZ and Z_{dr} data from Figs. 7 (9.1° elevation), 9, and 11, respectively.*
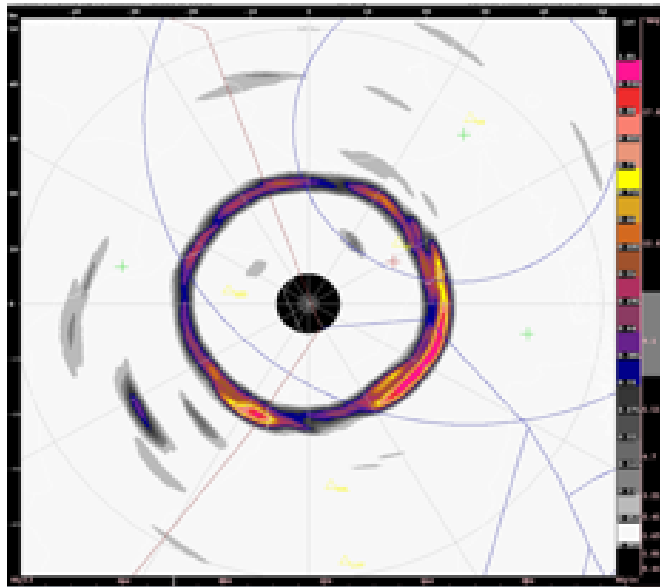

Figure 13: *PPI ring feature data corresponding to Fig. 12 except that the data have been smoothed.*
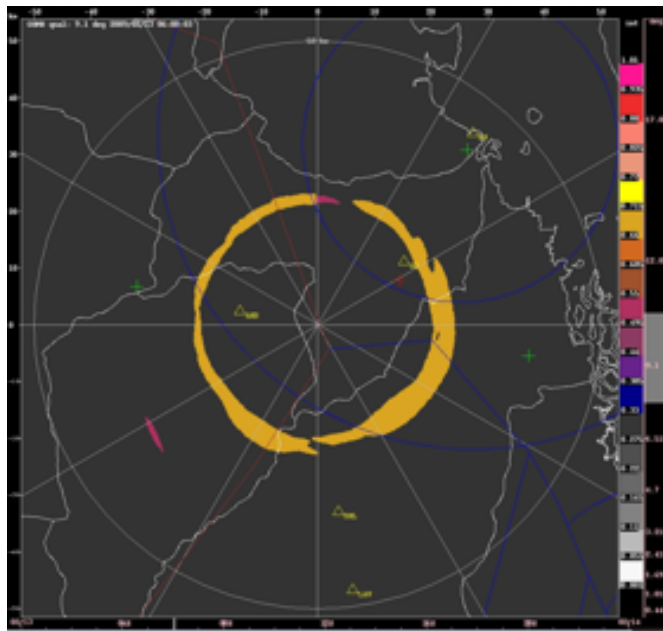
Figure 14: *PPI data quality ring feature generated from a combination of the double ring filtered ρ_{hv}, dBZ and Z_{dr} data from Figs. 7 (9.1° elevation), 9, and 11, respectively. The color scale indicates the "quality" or "strength" of the ring feature.*

The approach outlined so far is applied to all elevation angle scans within each radar volume, resulting in a clump quality image for each elevation angle. In summary, for each elevation angle, these processes are applied:

1. double ring filter of ρ_{hv};

2. double ring filter of dBZ;

3. double ring filter of Z_{dr};

4. combine (1), (2), and (3) (maximum);

5. smooth; and

6. clump.

d Histogram Decomposition

Using the set of clump images (one for each elevation angle scan), a two dimensional histogram $P(z, \phi)$ is created where z is a histogram bin center specifying a range of heights from $z - dz/2$ to $z + dz/2$, with z taking on a discrete set of values:

$$z_0, z_0 + dz, z_0 + 2dz, ..., z_0 + n\, dz \tag{3}$$

and ϕ is one of the radar elevation angles that were scanned. The histogram is defined as:

$P(z, \phi)$ = percent of points in range $z - dz/2$ to $z + dz/2$ at radar elevation ϕ that are part of some clump.

i Quality Adjustment to Histogram Values Each clump has an assigned quality value. The higher the quality value, the more likely the clump location is a proxy for the freezing level. The histogram values are adjusted so as to give higher results in histogram bins in which the quality of the clumps is high. The adjusted histogram values are:

$$A(z, \phi) = P(z, \phi) * F_q(Q(z, \phi)) \tag{4}$$

where P is from above, $Q(z, \phi)$ is the maximum quality value in the (z, ϕ) bin, and F_q is a fuzzy function. Including F_q provides more flexibility to the freezing level identification algorithm.

ii Scan Consistency Adjustments to Histogram If one bin z_i dominates a particular elevation angle ϕ, i.e., $A(z_i, \phi) \gg A(z_j, \phi)$ for all other z_j, then based on this one elevation angle, the bin z_i is very likely to be the best choice of z as an estimate of melting level. If, however, more than one bin has similar A value, the confidence in any one choice of z-bin as an estimate of freezing level goes down. In such cases, the A values are modified (normalized) into rescaled (R) values:

$$R(z, \phi) = A(z, \phi)\, F_s(A(z, \phi)/S(\phi)) \tag{5}$$

Bar Color	Value	Meaning
blue	$P(z, \phi)$	Simple percent clump values
green	$A(z, \phi)$	Quality adjusted
red	$R(z, \phi)$	Scan consistency rescale

Table 1: *Definition table.*

where $S(\phi)$ is the sum of all bin values for the elevation ϕ:

$$S(\phi) = A(z_0, \phi) + A(z_0 + dz, \phi) + \ldots + A(z0 + n\,dz, \phi) \tag{6}$$

and F_s is another fuzzy function. Including the fuzzy function F_s provides more flexibility to the freezing level identification algorithm. Both F_s and F_q can be considered "tuning" parameters that are under development.

iii Visualizing the Histograms To visually represent the results of this three-step histogram construction, histograms are plotted with elevation angles vertically and the bins z horizontally. This gives an intuitive, visual and practical way to estimate the freezing level. Three bars are drawn in each bin, with color of bar indicating which of the three steps is being displayed: The highest elevation scan (17.82°) is at the bottom and lowest (0.44°) is at the top.

Show in Fig. 15 is a histogram plot for the example used thus far, with low resolution bins (0.5 km) on the horizontal axis. Looking at the 17.82° elevation, nearly all the points fall into $z = 3$ km bin. Smaller values show up at z=6-7km. As we move down in elevation angle scanned, high percentages appear in the histogram fairly consistently between $z = 2.5$ and $z = 3$ km, with no clumps present at the lowest 3 elevation angles. A close-up of the 17.82° elevation histogram is shown in Fig 16. The green (A or adjusted) values were boosted due to the medium to high quality of the clumps. The $z = 3.0$ km bin was boosted all the way to 1.0. As can be seen, this bin dominates the scan.

The red (R or rescaled) values show the dominating bin unchanged, and the remaining bins removed altogether based on the fuzzy function F_s, except for the $z = 6.5$ km bin, which was reduced almost to zero. The final histogram of R (red bars) shows that the 3.0 km bin is by far the most likely one as seen by the 17.82° scan.

e *Estimating the Freezing Level from the Histograms*

The final step is to compare histogram results from all the radar elevation angles to determine which bin (height) is the most likely freezing level, and what the quality estimate is for this bin, using consistency at different radar elevations and histogram values.

The best case would be if every radar elevation angle had one dominant bin with a large R histogram value, and all elevations angles had the same dominant bin. In an intermediate case the bins would drift a little bit but not too much as a function of elevation angle. In a bad case the bins would show large inconsistency at different elevations and/or would have low quality.

The approach is to select a start bin identified by that bin with the largest overall $R(z, \phi)$ value (for all ϕ and z). Next, contiguous elevation angles (both higher and lower elevation angles, if present) are
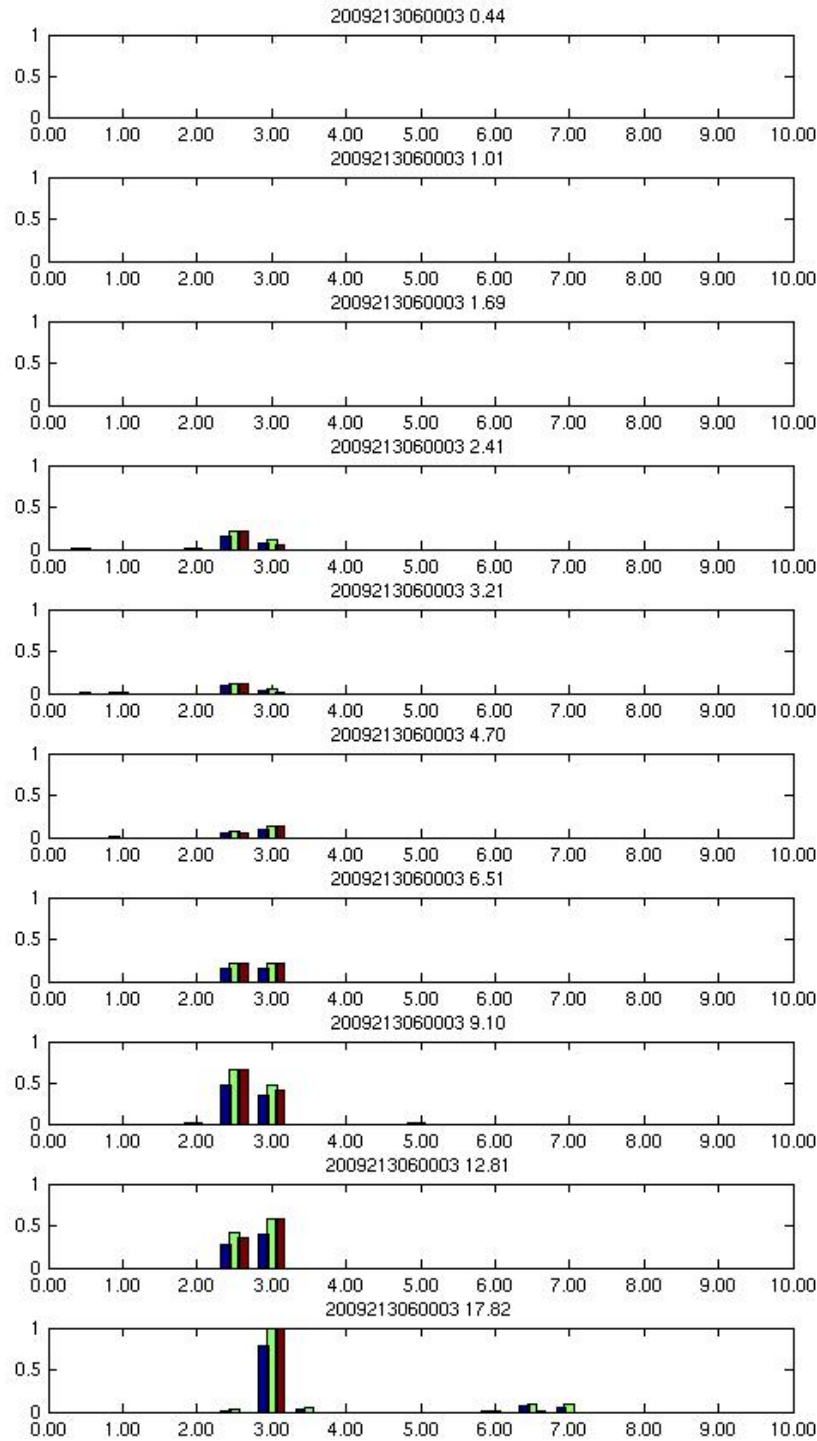
Figure 15: *Histograms of P, A and R values. Histogram arranged vertically by elevation angle and horizontal axis is height in kilometers MSL.*
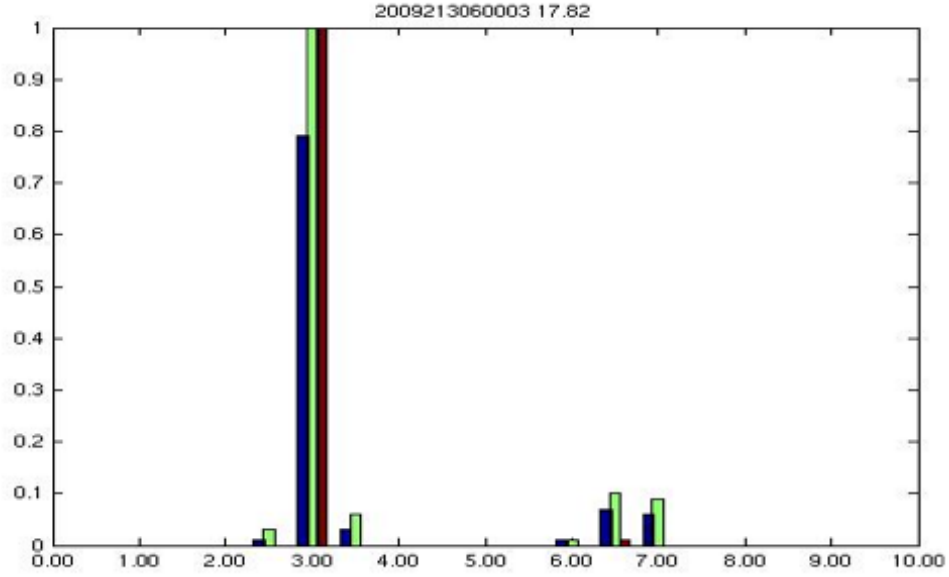
19

Figure 16: *Histogram of P, A and R values for the 17.8° elevation angle from Fig. 15.*

examined for high R values. Bins (heights) that are closer in distance to the previously selected bin are given higher weight (probability). Quality is initially given by the R value at the starting point, and it is adjusted based on what is seen at subsequent elevations. Higher quality values are assigned if there is a high R value bin with z unchanged or changing only slightly. Lower quality values are assigned if there are no high values of R at or nearby the previously selected z. A final step is to penalize if only a small number of elevations were included in the ridge.

In the histogram in Fig. 17, the ridge finding output has been added to the histogram of Fig. 15 as color-coded boxes with quality values and lines connecting them. In this example, the ridge is built starting at the maximum bin ($z = 3.0$ km, $\phi = 17.82°$), which is the histogram at the bottom of the figure. The starting point R value is shown within the green box close to the histogram. As we move up in the figure (down in elevation angle), the Q values are again shown in boxes drawn near the bin that was chosen. When the algorithm concludes, a red box is drawn with the final Q value within.

For this example, Table 2 gives the contents at each radar elevation, and a description of the action taken.
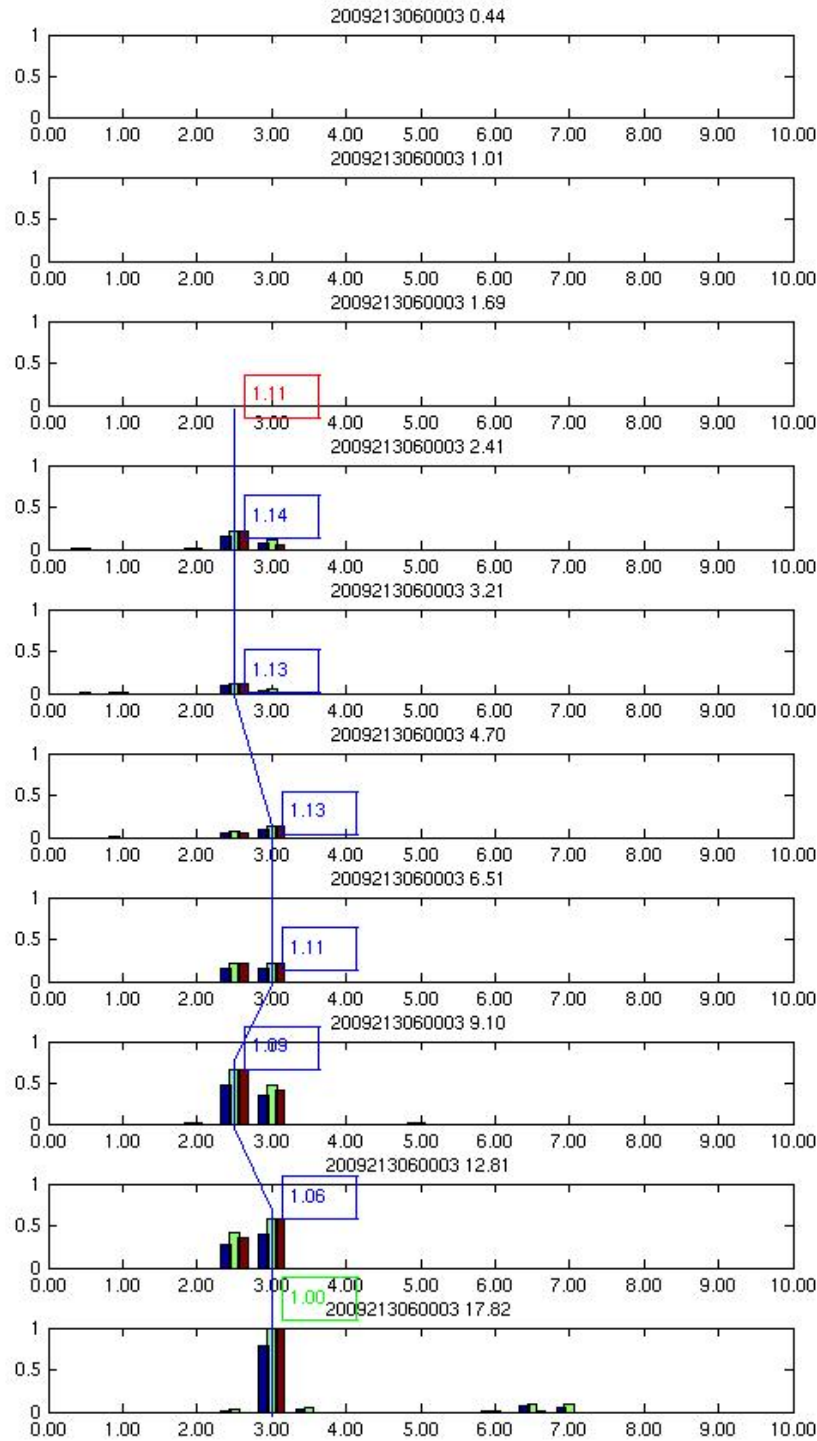
Figure 17: *Histograms of P, A and R values. Histograms are ordered vertically by elevation angle and horizontal axis is height (z) in kilometers MSL.* 21

ϕ (deg.)	**height** (z)	**Q**	Comments
17.82	3	1	Initial top quality from the entire histogram Zmax=3km R(3,17.82) = 1.0
12.81	3	1.06	Boosted, because it is the same bin as Zmax
9.1	2.5	1.09	Boosted because bin changed only 0.5 km
6.51	3	1.11	Boosted, same bin as Zmax
4.7	3	1.13	Boosted, same bin as Zmax
3.21	2.5	1.13	Boosted because bin changed by 0.5km, small because max at this elevation is small.
2.41	2.5	1.14	Boosted, bin change 0.5, and max value at this elev. is bigger.
1.69	2.5	1.11	Stopped here, quality reduced because still 3 elevations not in ridge.
1.01	2	–	Never evaluated, stopped above.
0.44	–	–	Never evaluated, stopped above.

Table 2: *Histogram values and the actions taken.*

f *Summary of Freezing Level Detection Algorithm*

The entire processing sequence goes as follows:

For each radar volume

    For each elevation angle scan

        double ring filter of ρ_{hv}

        double ring filter of dBZ

        double ring filter of Z_{dr}

        max combine

        smooth

        clump

    build a two-dimensional Histogram of percent clumped

    adjust for quality

    adjust for scan related consistency

    determine z, Q for this volume by doing ridge-finding
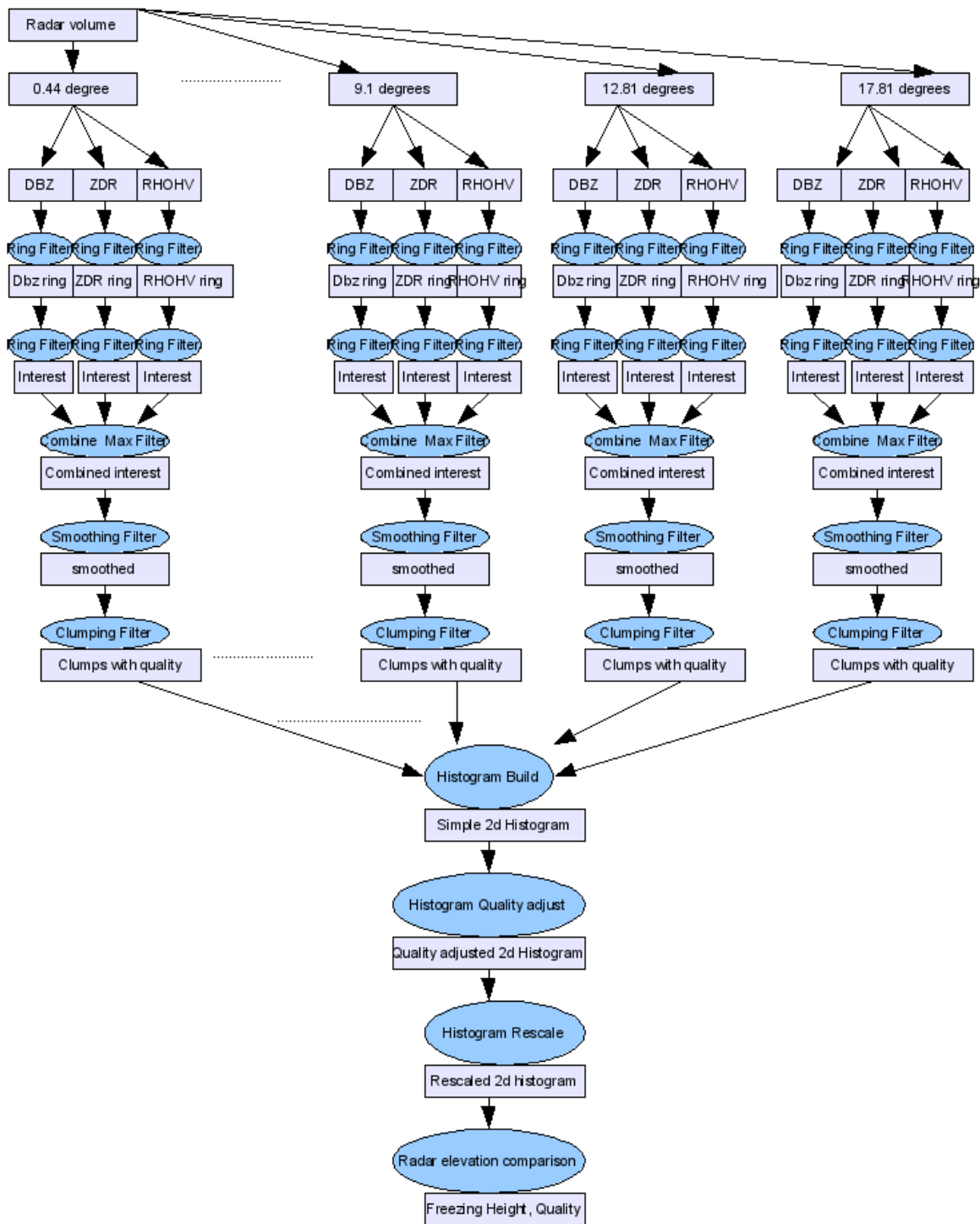
end

A data flow diagram is shown in Fig. 18.

Figure 18: *Flow diagram for the freezing level detection algorithm.*

g *A Second Data Example*

The previous example used radar data from a widespread stratiform precipitation case which exhibited a well defined bright band. The following case shows a fairly strong signal for more than one height Z. The dBZ and Z_{dr} PPIs are shown in Fig. 19 for the 6.51° elevation scan. Figure 20 shows results after the clumping process. Note the large number of clumps at a variety of radii. Similar behavior is seen at a number of elevation angles. The result is that the ridge-finding algorithm is not consistent and the quality is therefore slightly reduced, as can be seen in the histogram with ridge shown in Fig. 21.

i Time Series of Quality As radar volumes are processed, a time series plot of height Z and quality Q is possible. Figure 22 shows Z (blue) and Q (green) as a function of time. One can see a tendency to have higher quality during intervals with consistent Z values, and also that the time series indicates $Z = 2.5$ to 3km with a few estimates at 0.5 to 1.0 km.

ii Lag-Domain Statistical Representation A "lag-domain" approach can be used to identify consistent estimated freezing heights by plotting a 2-D histogram where the horizontal bin is given by $Z(t)$ and the vertical bin is given by $Z(t + 1)$ for a specified time interval t. If the Z value is consistent through time, a cluster (large count) will occur in the histogram at the particular Z. Figure 23 shows the the lag-domain histogram of the above time series.

As can be seen the time series shows clusters (large counts in red and orange) at 2.5 km and 3 km and a smaller cluster at (1km, 1km). The 1km data is seen early and late in the time series. The remaining areas with counts greater than zero are where the time series values are not constant. Based on this lag-domain representation, the freezing level is estimated to be in the 2.5 to 3-km height range.

The estimated data quality factor can be used as a threshold to sharpen the image. For example, if low quality threshold of 0.5 is used, the histogram values are almost entirely limited to (2.5km, 2.5km) and (3km, 3km). This is shown in Fig. 24.
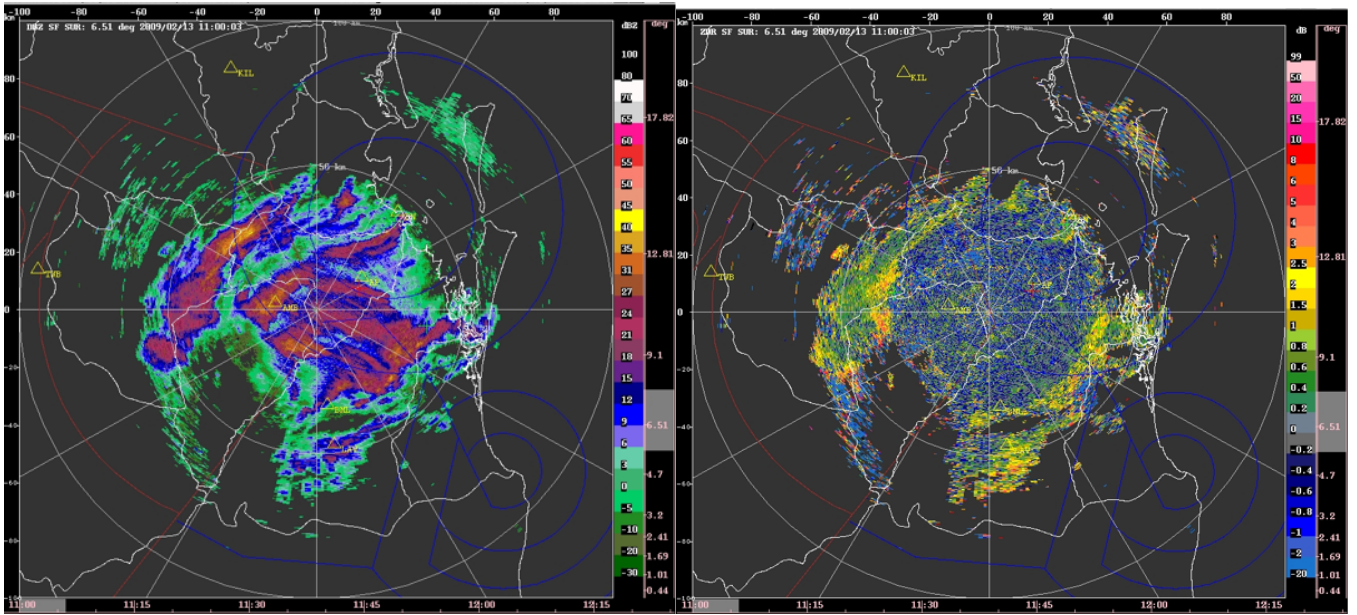
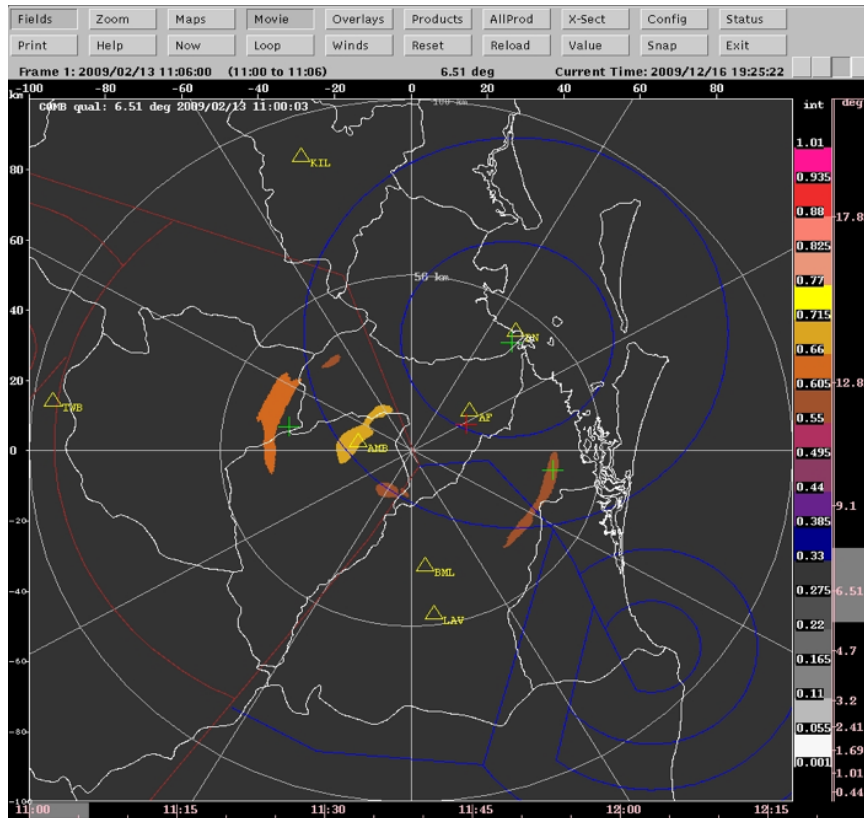Figure 19: *Reflectivity and Z_{dr} for the second example case.*

Figure 20: *Final results from the clumping process for the data in Fig. 19.*
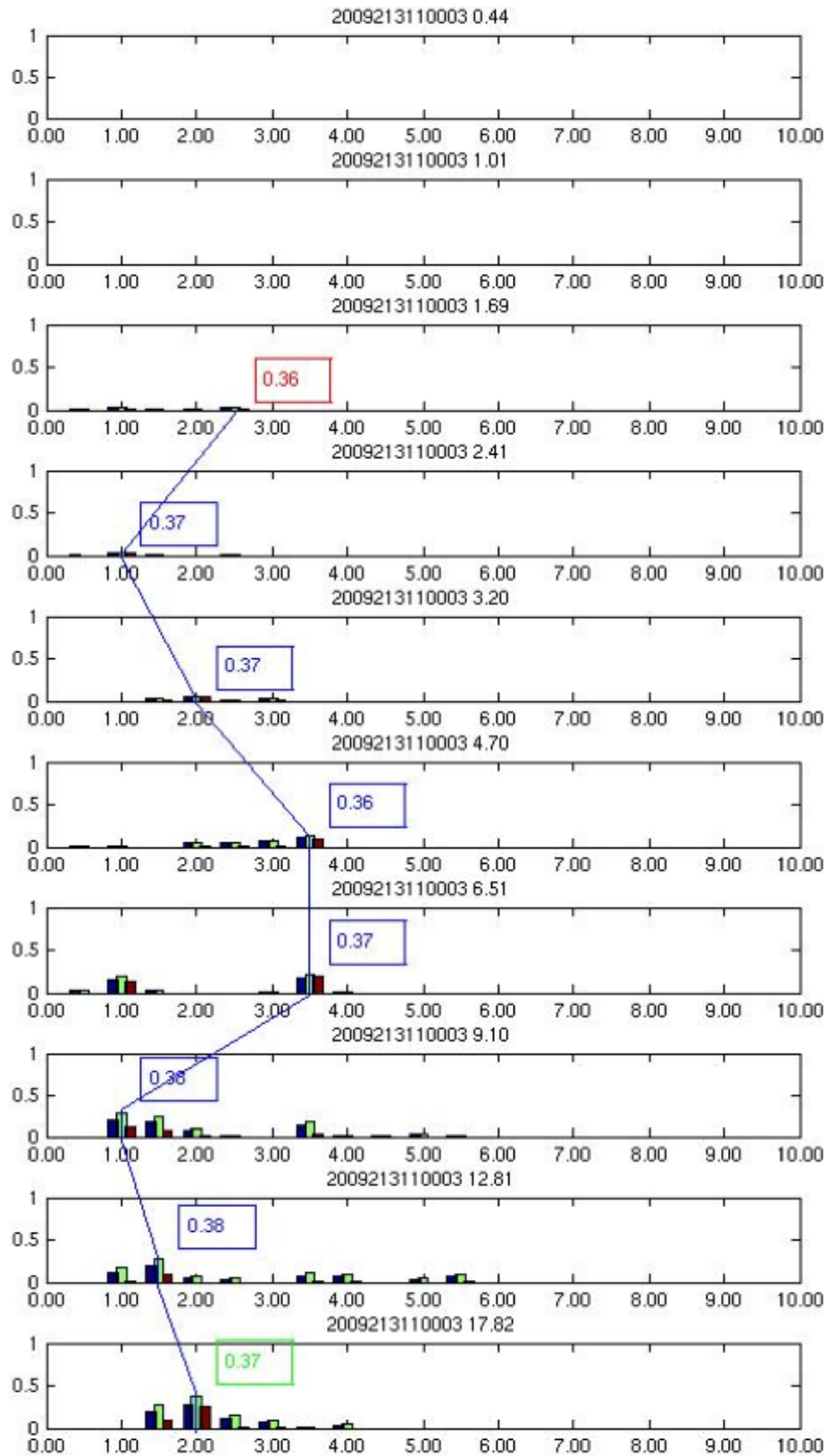
Figure 21: *Histograms of P, A and R values for the second data example. Histograms are ordered vertically by elevation angle and horizontal axis is height in kilometers.*
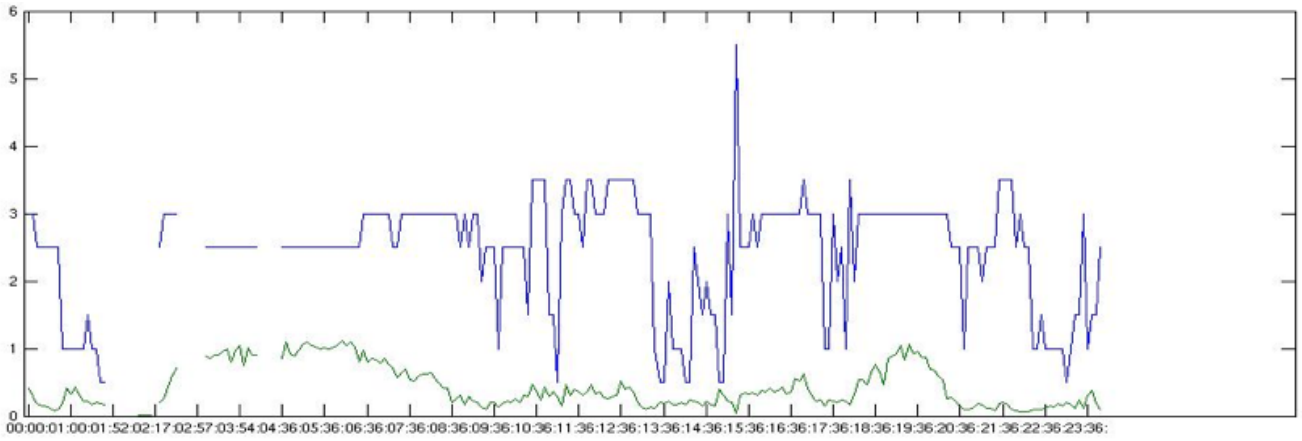
Figure 22: *A time series of selected possible freezing levels (blue curve) and associated quality factor Q (green curve). Vertical axis is height in km and and horizontal axis is time.*
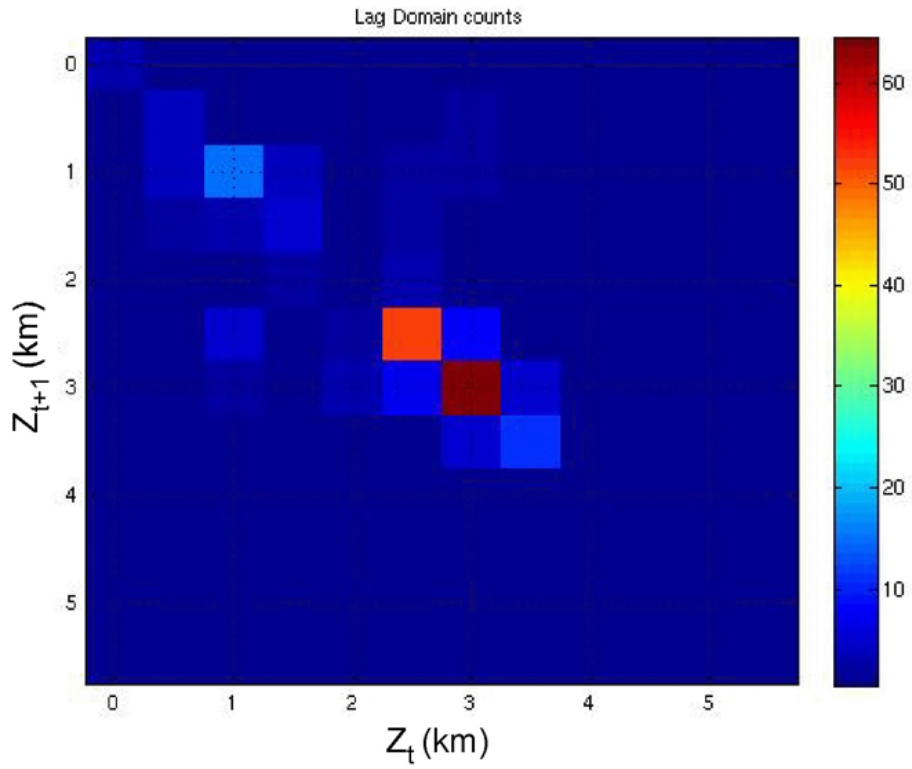

Figure 23: *A two-dimensional histogram of lag-domain values from the time series in Fig. 22.*
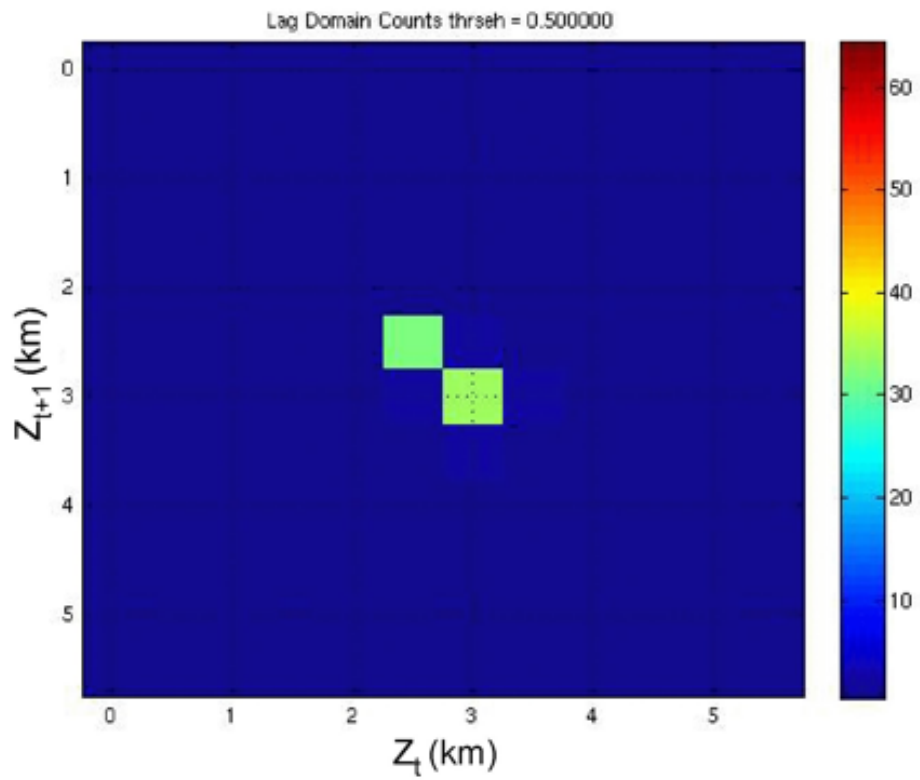
Figure 24: *The two-dimensional histogram of lag-domain values similar to Fig. 23 but with the calculated quality factor used to sharpen the image.*

h *Further Development*

Many areas can be explored using the techniques developed thus far.

1. Algorithm tuning: The various parameters have been initialized to reasonable values, but only a few cases have been processed, and the effect of parameter change is an area for additional research. Processing on a variety of data cases should be included in this research.

2. Real time output: The algorithm produces the time series output seen above, and also an accumulated Z value in the lag-domain. Use of these results is an area still to be determined.

3. Additional inputs: Any other fields that show ring like patterns can be added.

4. Differences between fields: It might be that some fields have different heights with the ring pattern for the same scan. The ability to handle this has not been included in the algorithm thus far.

5. Additional measures of freezing height: Ring patterns are only one approach. Other attributes of particular fields might show up in the freezing layer. Any technique that leads to an interest image with skill can be easily added. One example is texture, which may show different characteristics in the freezing layer.

6 Putting It All Together

The information and algorithms discussed thus far are now integrated to create an initial IHLA. The FLDA described above is used to make an initial estimate of the freezing level. An adjusted freezing level is estimated by combining this estimate with the temperature profile from a sounding (or the RUC). This new freezing level is used as in input to the PID. The PID is used to discriminate precipitation regions from non-meteorological data. Various spatial textures are calculated over the the areas occupied by hydrometeors. The information from the PID, RUC and the new texture variables are then combined in a fuzzy logic algorithm and indicates the icing condition likelihood.

7 Using Texture Features

Texture-related computations can be used to produce a freezing drizzle estimate by way of combining the results of the NEXRAD Drizzle Detection algorithm (NDDA) that takes advantage of previously developed algorithms FLDA, SndFzAdjust (an algorithm that modifies the freezing level calculated by the above describe freezing level detection algorithm), and PID.

The FLDA described previously ultimately produces a time series of freezing heights with associated confidence values. A time series example is shown in Fig. 25 for a case from CSU-CHILL radar data gathered on 27-28 October 2009. The blue line is the freezing height (km MSL), the green line is confidence and the red line marks ground level. As the confidence becomes very low near the end of the time series, the estimated freezing height becomes variable, which indicates weak and non-distinct freezing level signatures. For example, there are some ring-type features at heights near 5 km MSL. At least for
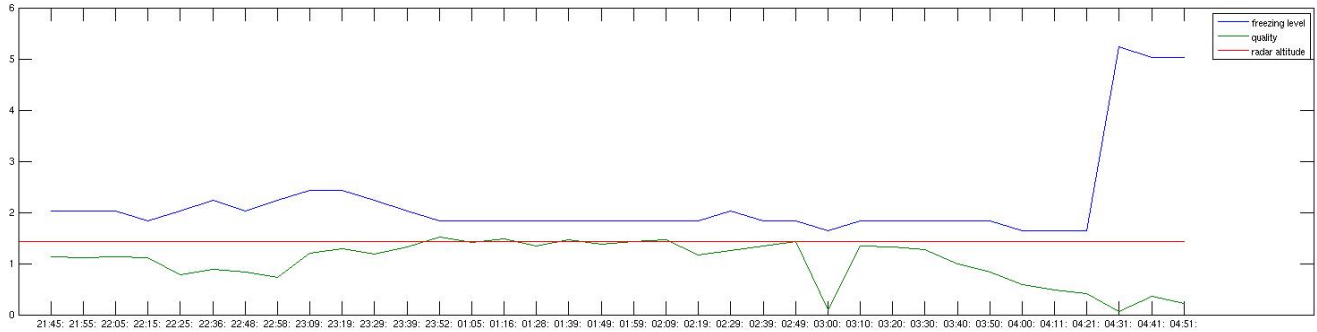
Figure 25: *A time series of CSU-CHILL data showing the freezing level estimates in blue. Vertical axis shows kilometers above MSL. The red line shows the ground level.*

the Front Range of Colorado, such estimates of freezing level can be discarded as extremely unlikely (unless inside a convective cell). Such high altitude ring signatures may be indicative of some type of precipitation layer, such as ice crystals, which could be of value in an IHLA. The majority of the case, though, shows a freezing height near 2 km MSL (CSU-CHILL is at 1.43 km MSL).

A good radar data example from this time period (i.e., high quality ring estimate) from CSU-CHILL data gathered at 02:29:42 28 October 2009 at 8.14° elevation angle is shown in Figs. 26 and 27. The final ring estimate is seen close in by the radar location.

We next examine data from the end of the time series in Fig. 25 where the freezing level estimate was about 5 km MSL. Shown in Figs. 28 and 29 is data from 04:51:37 at 8.14° elevation. Now there is no ring signature found close to the radar and there is only a small portion of a ring in the lower left quadrant (Fig. 27). At this time snow was observed falling at the surface and thus the freezing level had descended to ground level. The small ring signature seen at this time likely is due to oriented ice particles. This is further supported by the positive Z_{dr} values in this area in Fig. 28.

8 Prototype IHLA

We now begin to put some of the pieces of the puzzle together for an IHLA. As a first step the technology developed thus far is combined with the NDDA.

An important input to the PID is the local sounding data and the correct 0° level. Soundings are infrequent and may not be accurate. An initial sounding adjustment algorithm, the SndFzAdjust algorithm, was made that uses the freezing level estimate to adjust the sounding data. The adjusted sounding is then fed into the PID algorithm, which categorizes all the radar echoes. The PID output is used to mask portions of the radar data. The masked radar data is then used as input to the NDDA algorithm, which has many intermediate derivations leading to one final number: the estimate of freezing drizzle likelihood. A block diagram of these steps is given in Fig. 30.

We now show an example of each step of this process for elevation angle = 2.71° for the data shown above at time 02:29:42. The ring pattern for elevation 2.71° is shown in Fig. 31 and the accompanying histogram plot is given in Fig. 32. This yields a freezing height estimate of approximately 2 km MSL.
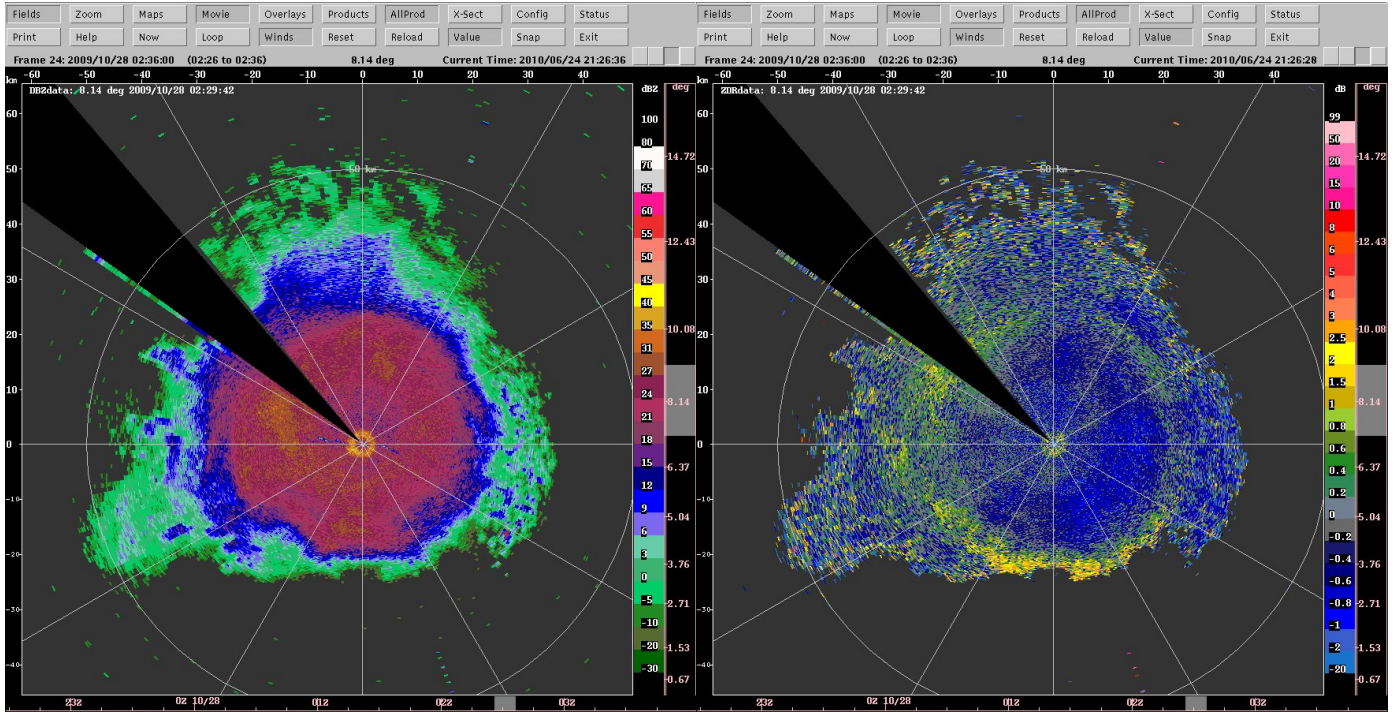
Figure 26: *dBZ and Z_{dr} from CSU-CHILL data gathered at 02:29:42 28 October 2009 at 8.14° elevation angle.*
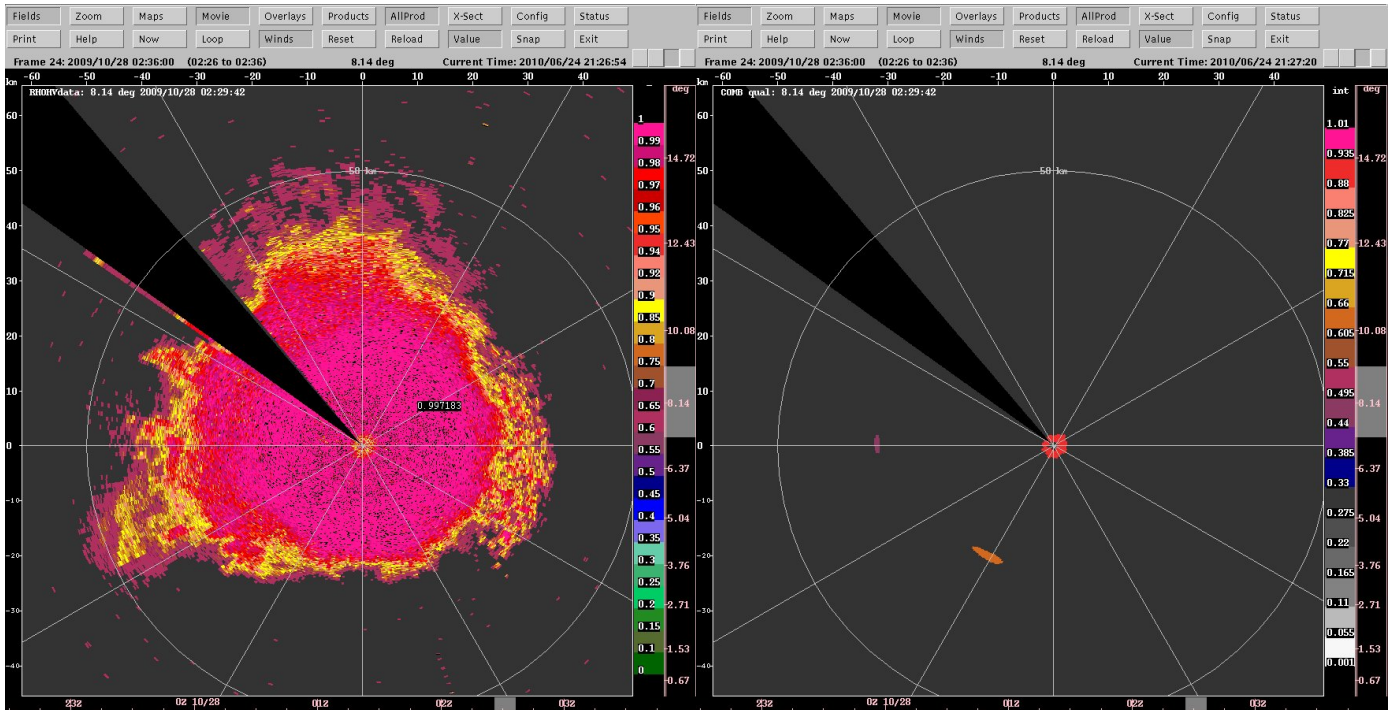
.

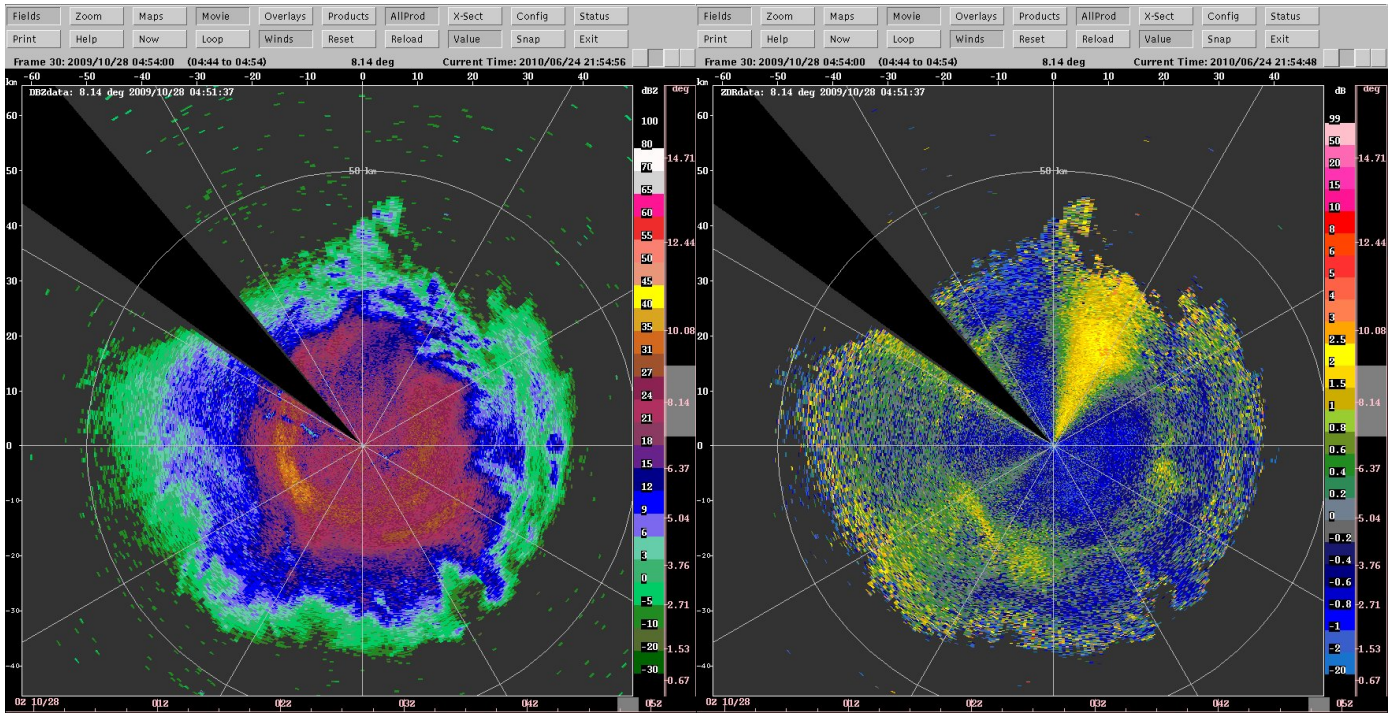Figure 27: *ρ_{hv} and the final ring estimate accompanying the data of Fig. 26.*

Figure 28: *dBZ and Z_{dr} from CSU-CHILL data gathered at 04:51:37, 28 October 2009 at 8.14° elevation angle.*
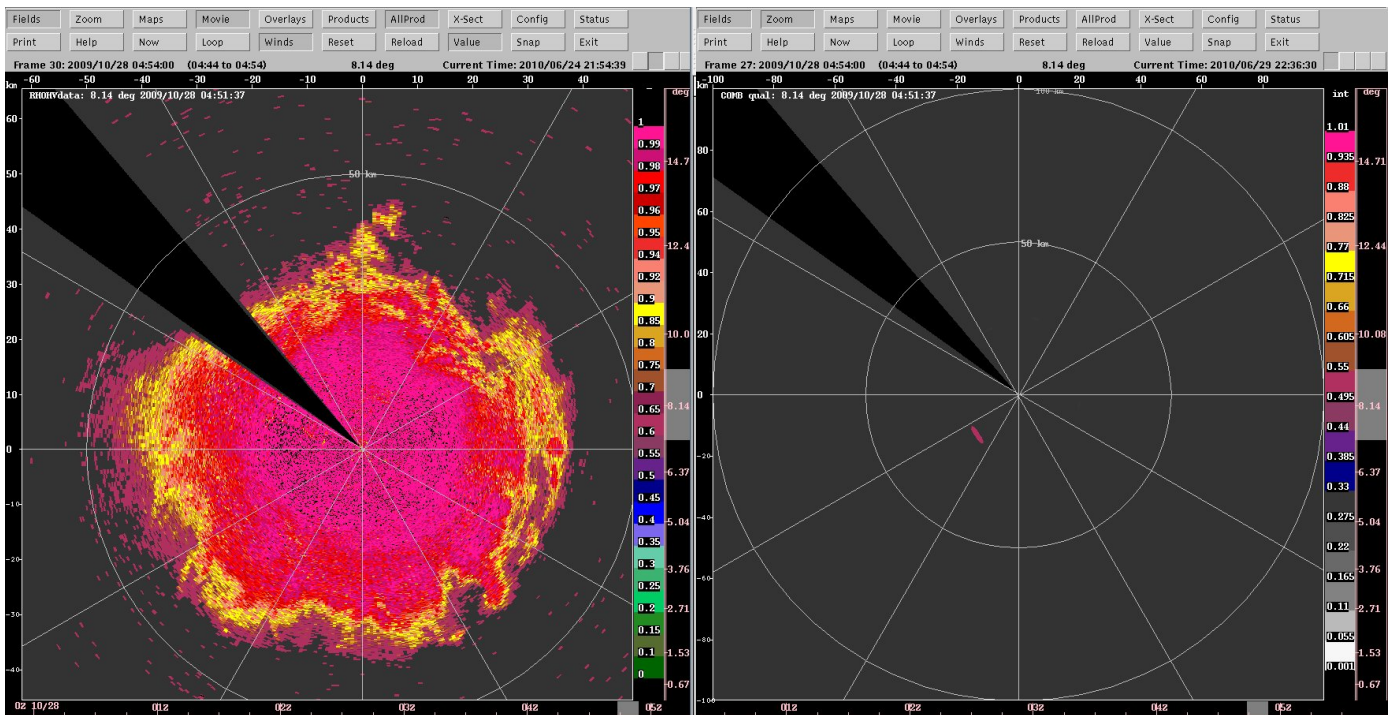

Figure 29: *ρ_{hv} and the final ring estimate accompanying the data of Fig. 28.*
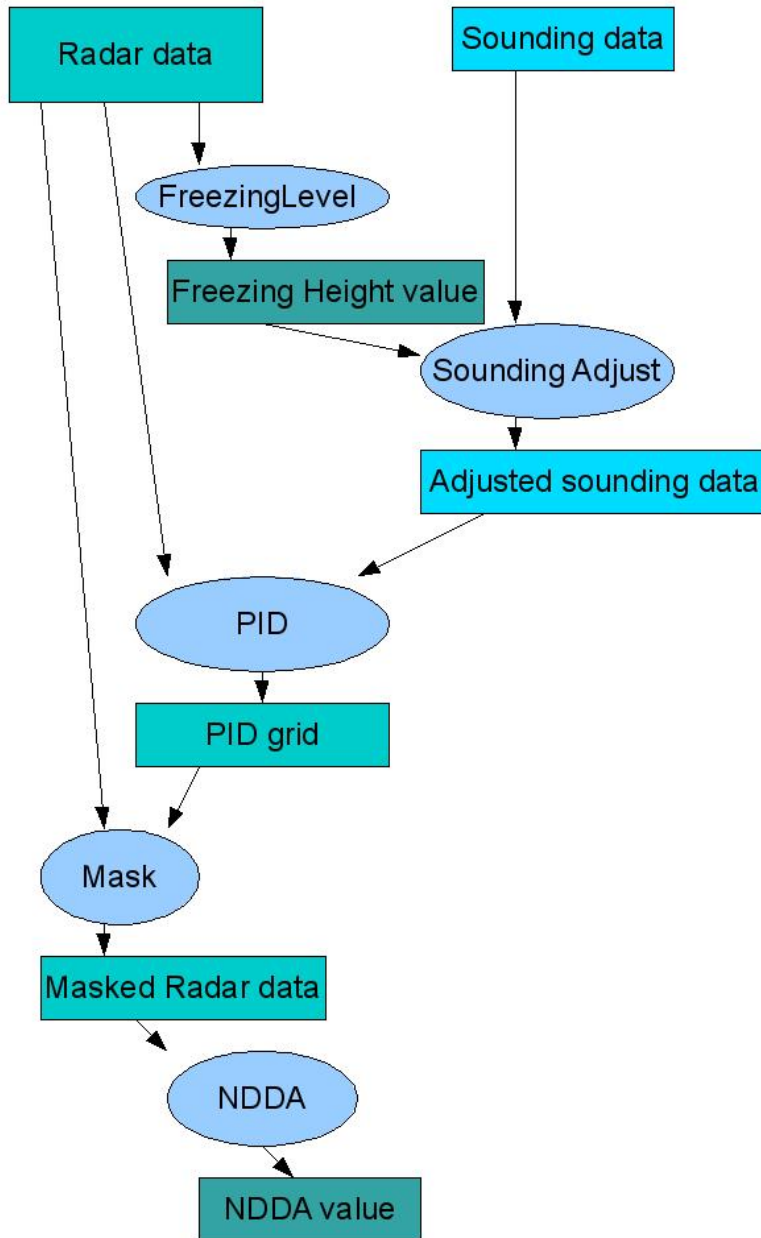
Figure 30: *Block diagram of of the data processing that occurs before radar data is fed to NDDA.*
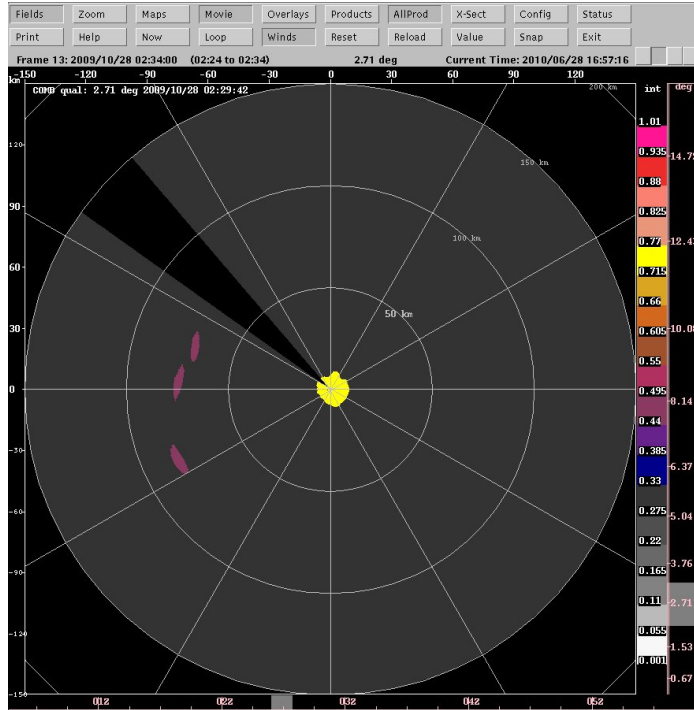
Figure 31: *The final estimate from the ring filter process for CSU-CHILL gathered at 02:29:42*

.

This freezing height is used by SndFzAdjust to adjust the sounding data. The sounding data is used by PID to produce its output. The results of PID with and without using the SndFzAdjust adjustment is shown in Fig. 33.

The PID categories considered for investigating the presence of freezing drizzle are SLW, Irreg-ice, ice, and dry snow. All other types are masked out. For the present case we show dBZ without and with this masking applied in Fig. 34.

The masked dBZ field is then fed to the NDDA which calculates a freezing drizzle likelihood estimate. The mean and median fields are computed for use in NDDA over small two-dimensional averaging windows and are shown in Fig. 35. The remaining fields are all single numbers, so a time series is a nicer way to represent what happens to produce the final value.

The NEXRAD Drizzle Detection Algorithm (NDDA) was developed by Ikeda et al. (2009) to detect freezing drizzle using NEXRAD data. A detailed description of the algorithm, results and scientific motivation can be found in the paper. The following discussion is a synopsis of the algorithm described in the Ikeda et al. (2009).

The algorithm calculates numerous statistical measures and uses fuzzy logic to convert these measures into scores; the individual scores are then combined into a single final score. If the final score is above a threshold freezing drizzle is inferred to be present in the scan. The statistical measures calculated are the median reflectivity, the global standard deviation of the reflectivity, the median of the local standard deviation of the reflectivity, the standard variation of the local standard deviation of the reflectivity, and the median reflectivity of the local texture. Notice the statistical measures are single values calculated
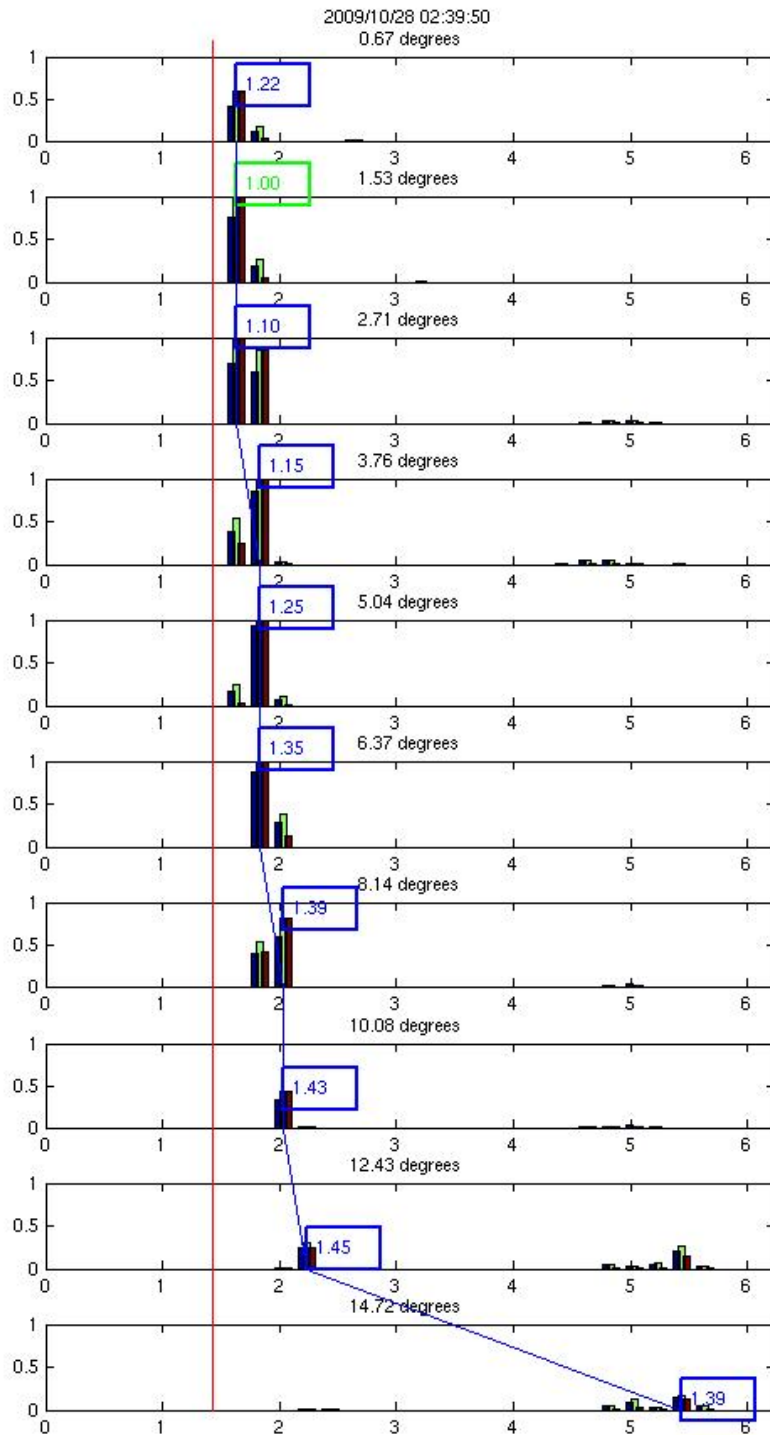
Figure 32: *Histograms of P, A and R values. The histograms are vertically arranged by elevation angle and horizontal axis is height (z) in kilometers (MSL). The red line is ground level.*
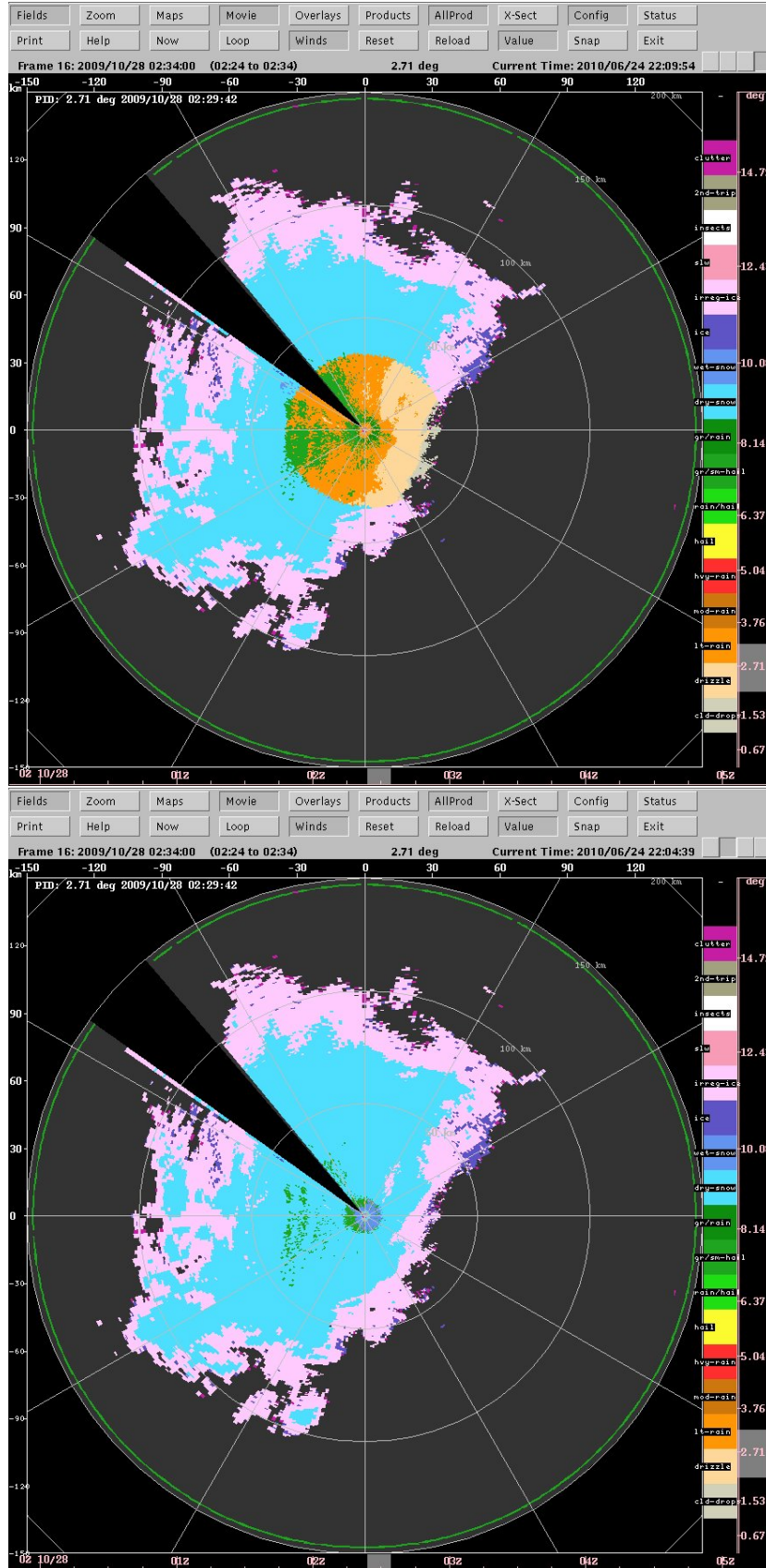
Figure 33: *An example of PID output for without the sounding adjustment (above) and with the sounding adjustment (below).*
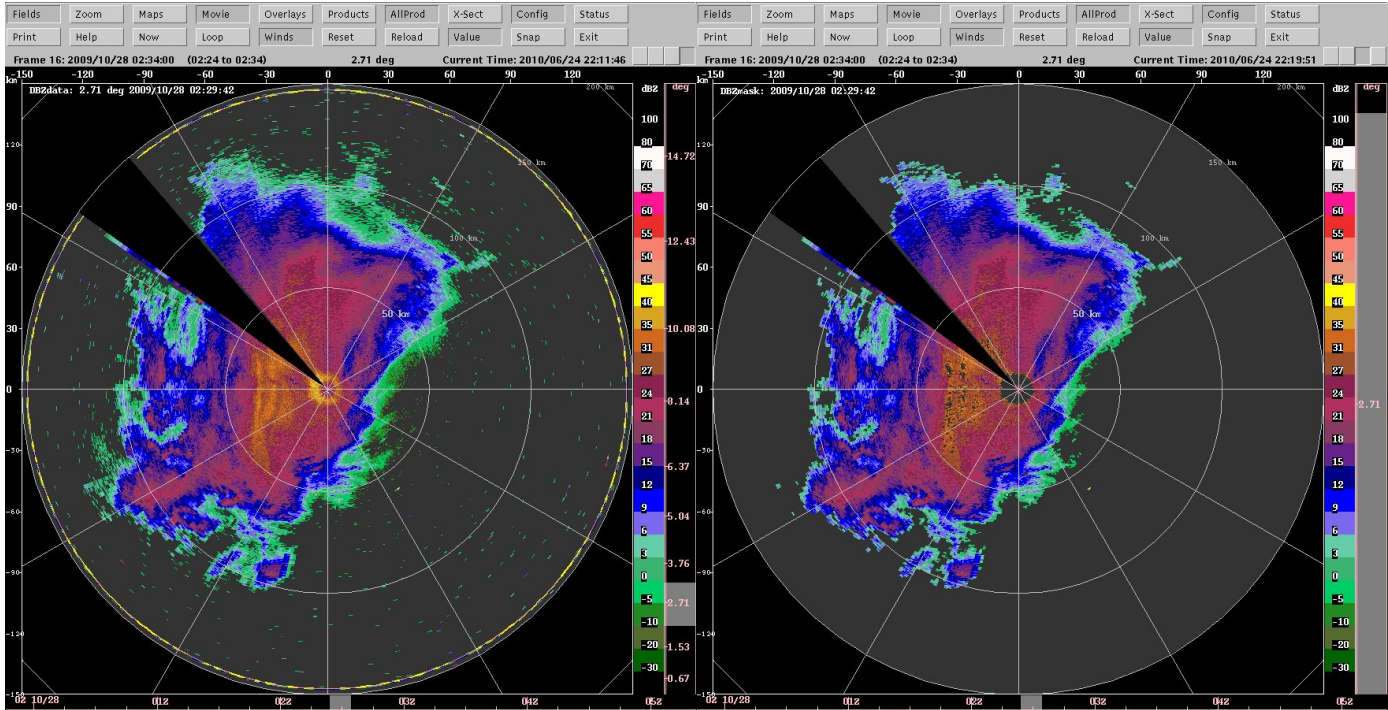
36

Figure 34: *Reflectivity from 02:29:42: Left, without PID masking. Right, with PID masking.*

over a domain. For the purposes of the algorithm, there are two domains, a near domain (15 km) and a far domain (100 km). Consequently, there are a total of tenscores that are combined to determine the final score.

To implement the algorithm one needs to calculate the median and standard deviation of a 2-D field over a specified range and azimuth domain, calculate a standard deviation over a local range and azimuth region, calculate a texture over a local range and azimuth region. Finally, code is needed to remap the output statistics into scores using piecewise linear functions (fuzzy membership functions).

The local texture and standard deviation are calculated by Eqs.(1) and (2), respectively. Figure 35 illustrates the local standard deviation (left panel) and the local texture (right panel).

Figure 37 shows a block diagram of the processing needed to calculate the final NDDA score (assuming the PID has already been calculated and applied to the input reflectivity data). The output of the remap functions is shown as a time series in the Fig. 38. The fuzzy membership functions are shown in Figure 2.
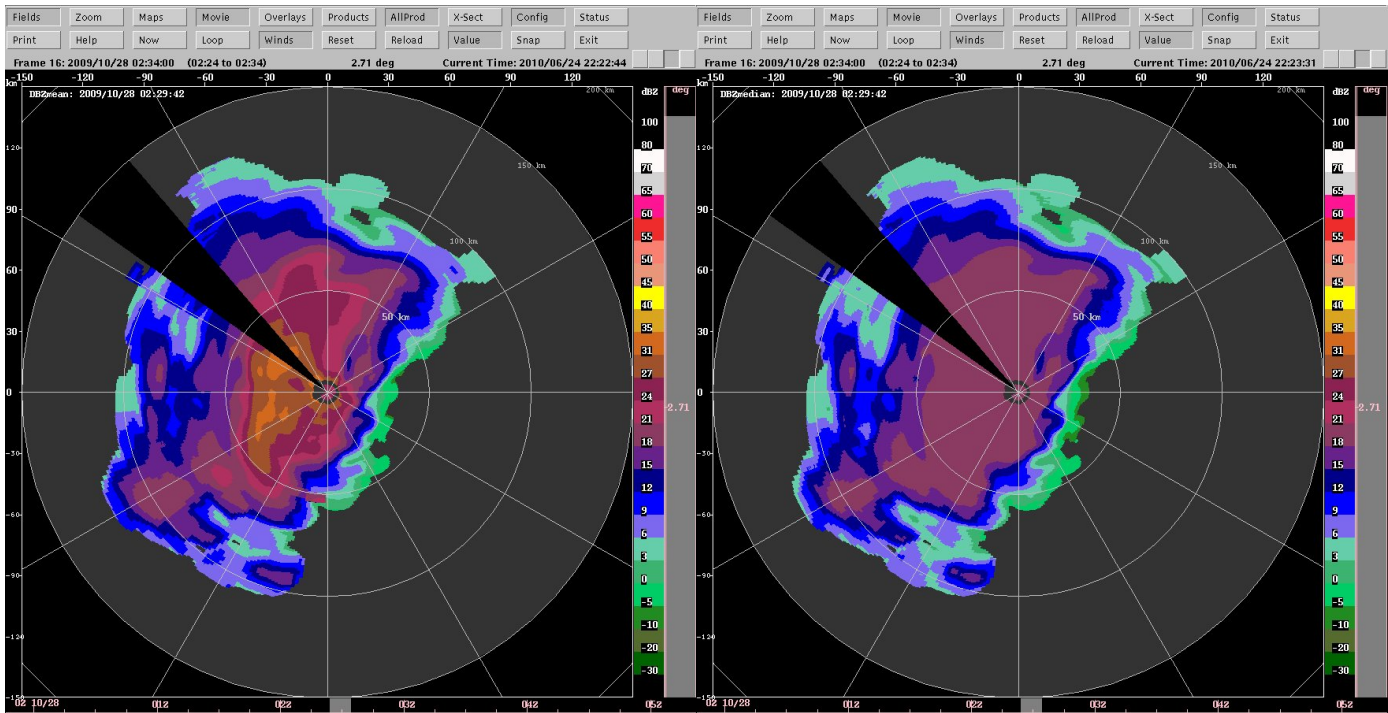
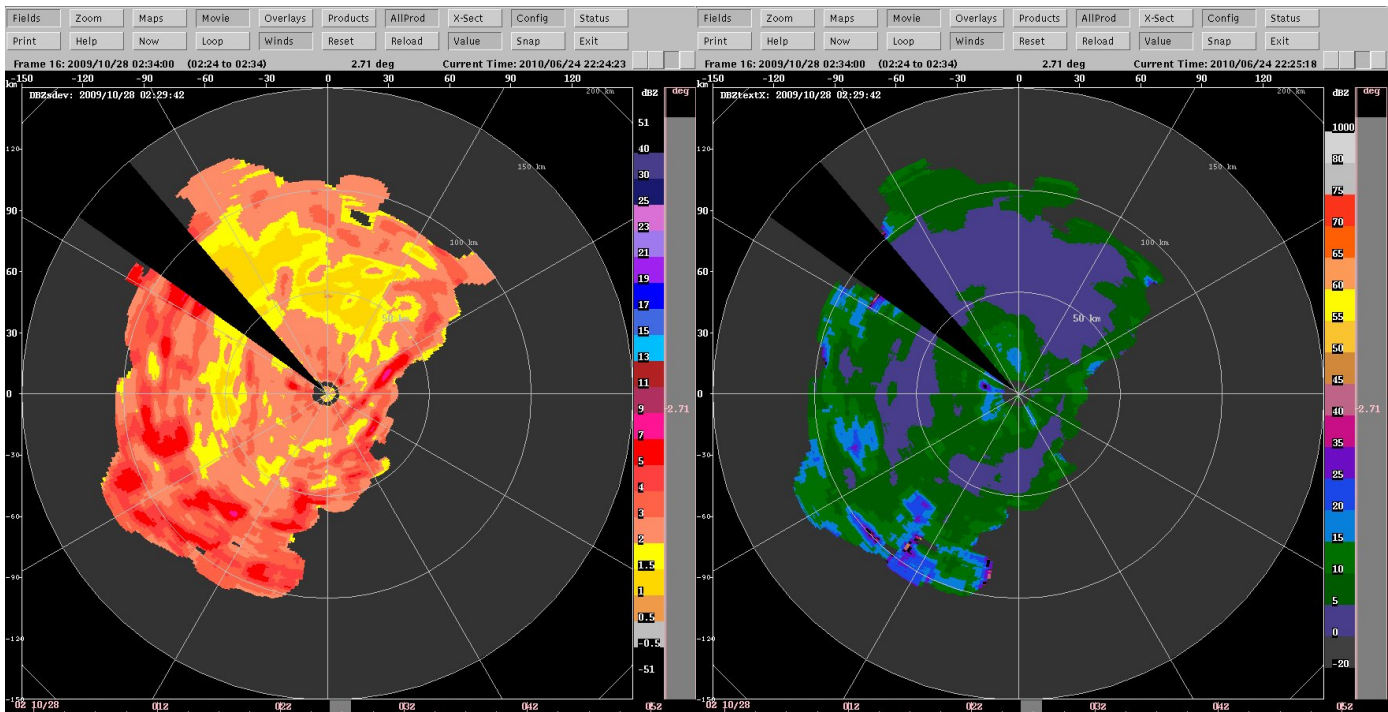Figure 35: *The mean and median dBZ fields computed for use in NDDA.*

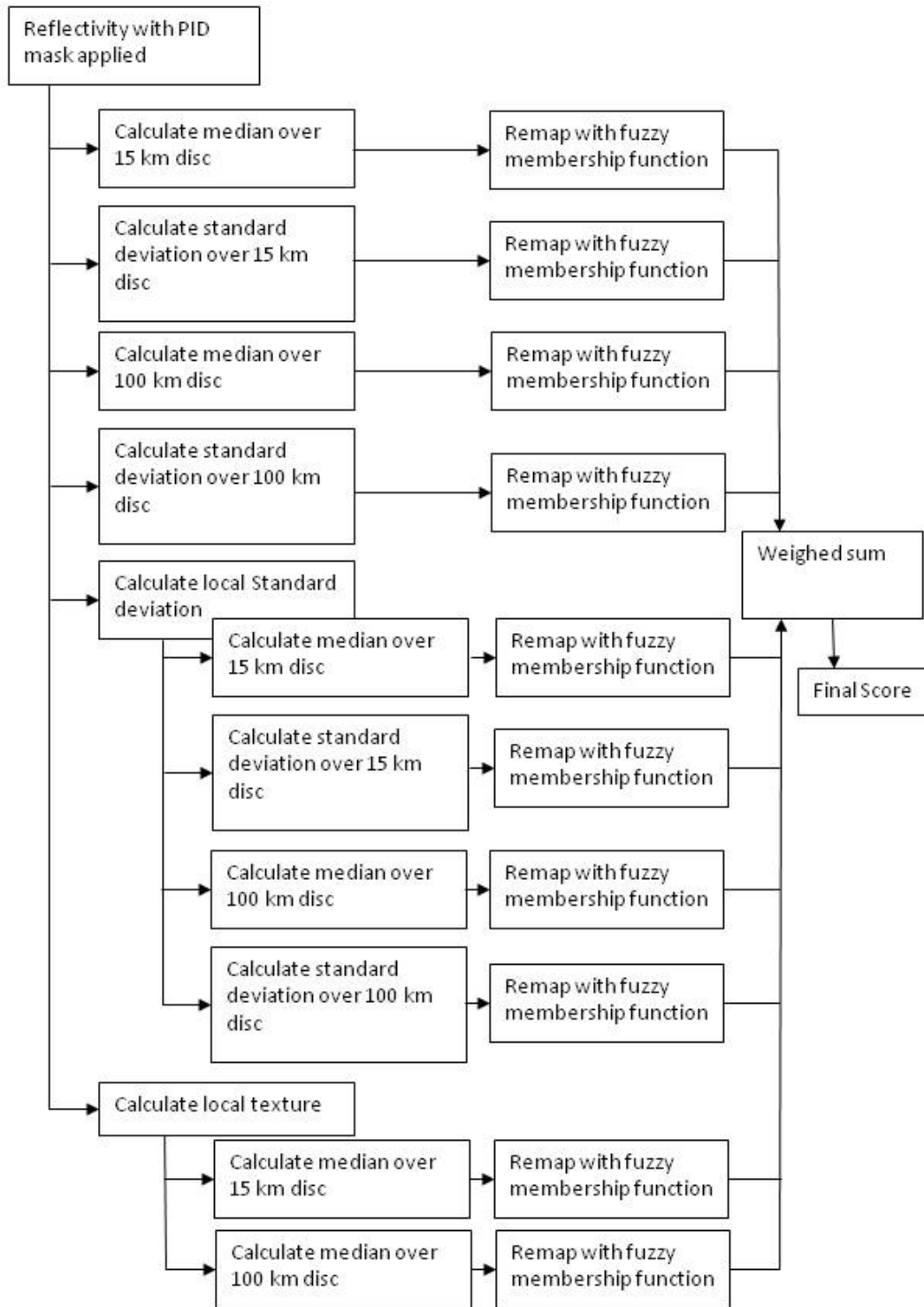Figure 36: *Standard deviation and texture of dBZ.*
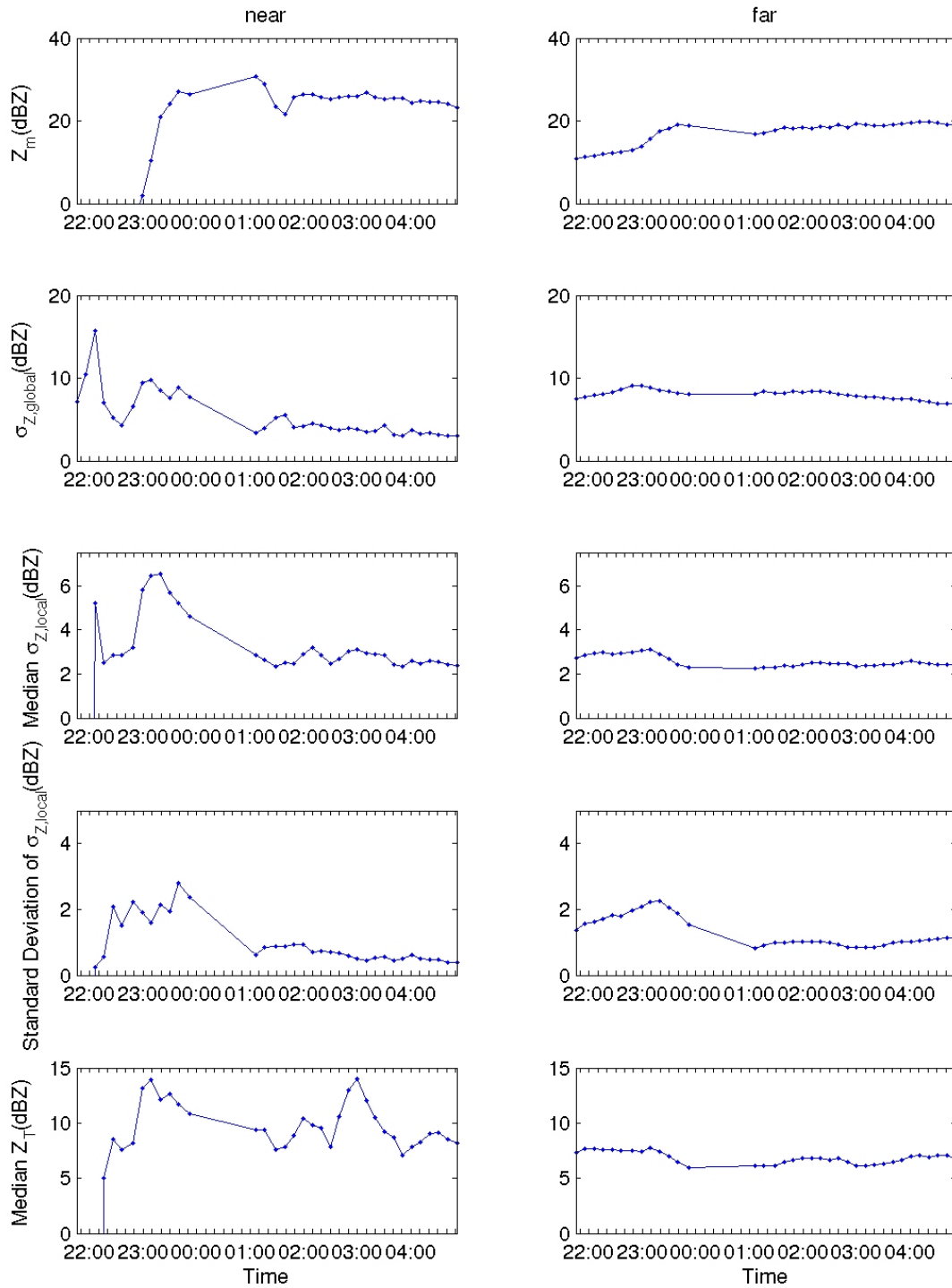
Figure 37: *Block diagram of NDDA.*

Figure 38: *Time series of NDDA parameters.*

9 Preliminary Fuzzy Logic Icing Detection

a *Introduction*

In the previous section, a preliminary IHLA was constructed by simply using the freezing drizzle detection algorithm (NDDA) from Ikeda et al. (2009). The NDDA is shown in the flow chart in Fig. 30. Obviously, detecting freezing drizzle at ground level is substantially different from detecting aircraft icing conditions aloft. In this section we begin to expand the NDDA into an algorithm more appropriate for aircraft icing condition detection aloft.

The data set used in this part of the study was observed with the CSU-CHILL radar near Greeley Colorado on 28 October, 2009. On this day there were several pilot reports of icing in the Front Range Colorado region including Denver International Airport (DEN), Greeley Airport (GXY) and the Front Range Airport in Broomfield (BJC). The pilot icing reports ranged from light to moderate-severe at flight levels between 9000 to 15000 ft above MSL. Taking into account normal atmospheric propagation using the 4/3 Earth radius approximation (Rinehart 2004), the elevation of CHILL (1.43 km), and converting to km, the flight level range of the icing reports corresponds to the range of about 1.3 to 3.1 km above the CHILL radar. Therefore this is a good case to test the radar variables and a preliminary algorithm.

The 28 October data are from an upslope stratiform case. The reflectivity (dBZ, top panel), differential reflectivity (Z_{dr}, middle panel) and specific differential phase (K_{dp}, bottom panel) at 02:29 UTC at an elevation angle of 1.53 are shown in Fig. 39. The time was chosen because it is central to the pilot icing reports and therefore most likely to manifest icing conditions. The data have been masked as described above (note that the wedge of missing data extending to the northwest of the radar were missing from the original data set and not edited by the algorithm). Widespread echo can be seen with distinct features in the dBZ, Z_{dr} and K_{dp} fields. There is a band of higher dBZ oriented in the north-south direction and is near collocated locally with high Z_{dr} and K_{dp}. At $1.53°$ elevation the ranges that correspond to the span of heights of the pilot icing reports are from 40 km to 95 km.

Two studies found in the literature were utilized to produce fuzzy logic icing potential product. The first study is from Ikeda et al. (2009) which utilizes fields derived from reflectivity (dBZ) to determine if there is freezing drizzle at ground level. The algorithm is modified here to identify supercooled large drops (SLD) above the ground. The second study by Plummer et al. (2010) examines the utility of dual-polarization variables to discriminate mixed-phase from ice-only conditions. Although Plummer et al. (2010) do not propose an algorithm, their findings are adapted into a preliminary algorithm and applied to the CHILL data.

Therefore we are developing separate algorithms to detect icing in different conditions. The results of the algorithms will need to be combined and the icing information displayed in a manner that is useful to the end users. The algorithms discussed here would replace the light blue oval labeled NDDA in the block diagram shown in Fig. 30. The combined output of these algorithms would replace the green rectangle labeled NDDA value. Determining the most effective representation of the icing detection results needs to be defined in the context of end users.

It is important to keep in mind that there may be vastly different cloud processes resulting in icing and with different radar signatures than those reported by Ikeda et al. (2009) and Plummer et al. (2010). A radar-based icing detection algorithm needs to have the flexibility to incorporate different radar signatures
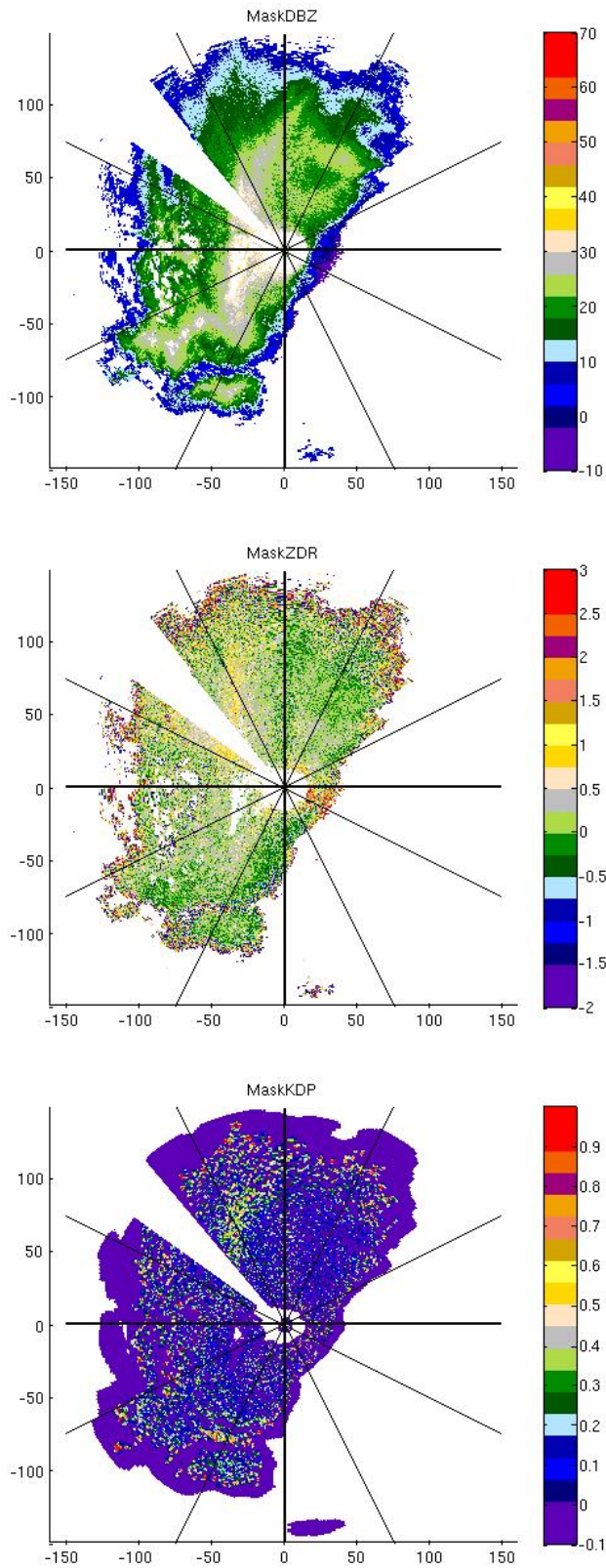
41

Figure 39: *Reflectivity (top), differential reflectivity (middle) and specific differential phase (bottom) from CHILL on 28 October at 02:29 UTC. The data have been masked using the algorithm described above.*

of different phenomena. This is an important goal of this work and the two studies utilized to date are considered a good starting place.

b *Identifying Supercooled Water*

The algorithm of Ikeda et al. (2009) was designed and tested to detect freezing drizzle at the ground. Therefore if the principles shown by Ikeda et al. (2009) are to be used for detection of in-flight icing conditions, the algorithm must be modified and extended to be applicable at altitudes above the ground. Ikeda et al. (2009) used the region within 15-km radar range ring to compute the characteristics of the measurements in the layer closest to the ground using the 1.5° elevation angle scan. Here, this idea has been extended to 15-km width bands at successively farther ranges and thus higher elevation layers. For example the lowest layer is from 0 to 15 km radar range, the next layer is from 15 to 30 km radar range and then from 30 to 45 km and so on, similar to the suggestion by Ikeda et al (2009). Each 15-km radar range band at 1.53° elevation angle spans about 0.4 km in vertical height. This allows us to utilize the large region spatial variables of Ikeda et al. (2009) at various heights above the radar. Figure 40 shows examples of the standard deviation (top) and median (bottom) of the local standard deviation of dBZ computed over the 15-km width bands at 1.53° elevation angle. It can be seen that the lowest values, corresponding to higher likelihood of icing, occur within a range of about 75 km of the radar or 2.3 km above the radar. This is in general agreement with the pilot icing reports between 1.3 and 3.1 km above CHILL.

Another modification to the algorithm of Ikeda et al. (2009) in this preliminary study, is that we use directly as feature-fields the locally computed quantities that Ikeda et al. (2009) use to compute the feature fields in the large regions within the 15 and 100-km radar range rings. Ikeda et al. (2009) show that freezing drizzle has lower values of the locally-computed standard deviation and texture of the dBZ (sdevDBZ and TDBZ, respectively). They also show that the mean reflectivity value itself can have some information about the presence of freezing drizzle. Therefore these fields are tested to determine whether or not they can provide information concerning the spatial distributions of icing likelihood. Figure 41 shows the values of the local sdevDBZ (top panel) and TDBZ (middle panel) and the mean dBZ (bottom panel) computed following Ikeda et al. (2009). It can be seen that there are relatively low values of both sdevDBZ and TDBZ to the north of CHILL at ranges from roughly 50 to over 100 km and to the south of CHILL at about 50 to 75 km range. Again this is in qualitative agreement with the pilot icing reports around the time of the radar observations. The lower values (indicative of icing) of local sdevDBZ and TDBZ do not occur in regions with the largest values of the mean dBZ, but occur farther in range, and thus higher in altitude, to the largest dBZ values.

The five feature-fields described here seem consistent with the findings of Ikeda et al. (2009) considering the pilot icing reports. They are sdev(sdevDBZ), median(sdevDBZ), MeanDBZ, sdevDBZ, and TDBZ, where sdev(sdevDBZ) and median(sdevDBZ) refer to the layer-based standard deviation and median of the local standard deviation of dBZ described above. Therefore membership functions were designed to estimate the degree to which supercooled drops belonged to each feature-field based on the results from Ikeda et al. (2009). The result of applying the membership function to a feature-field is a number between 0 and 1, referred to as the interest value. An interest value of 1(0) indicating high(low) likelihood of SLD as indicated by the particular feature-field. The membership functions for MeanDBZ,
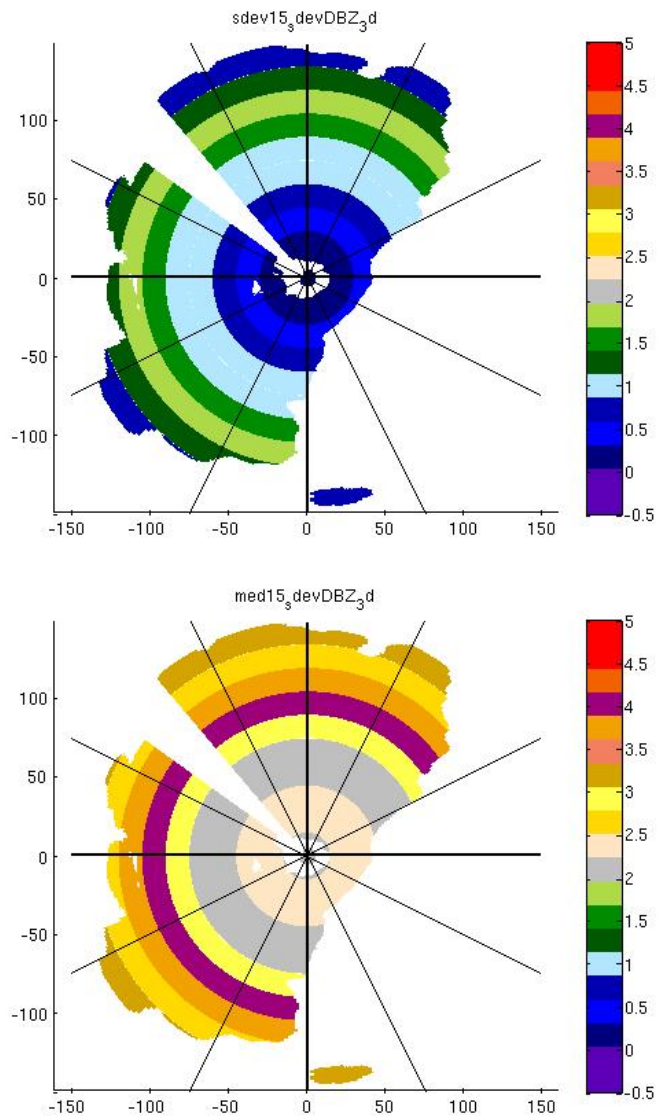
Figure 40: *Standard deviation (top), and median (bottom) of the local standard deviation of dBZ computed over 15-km width bands.*
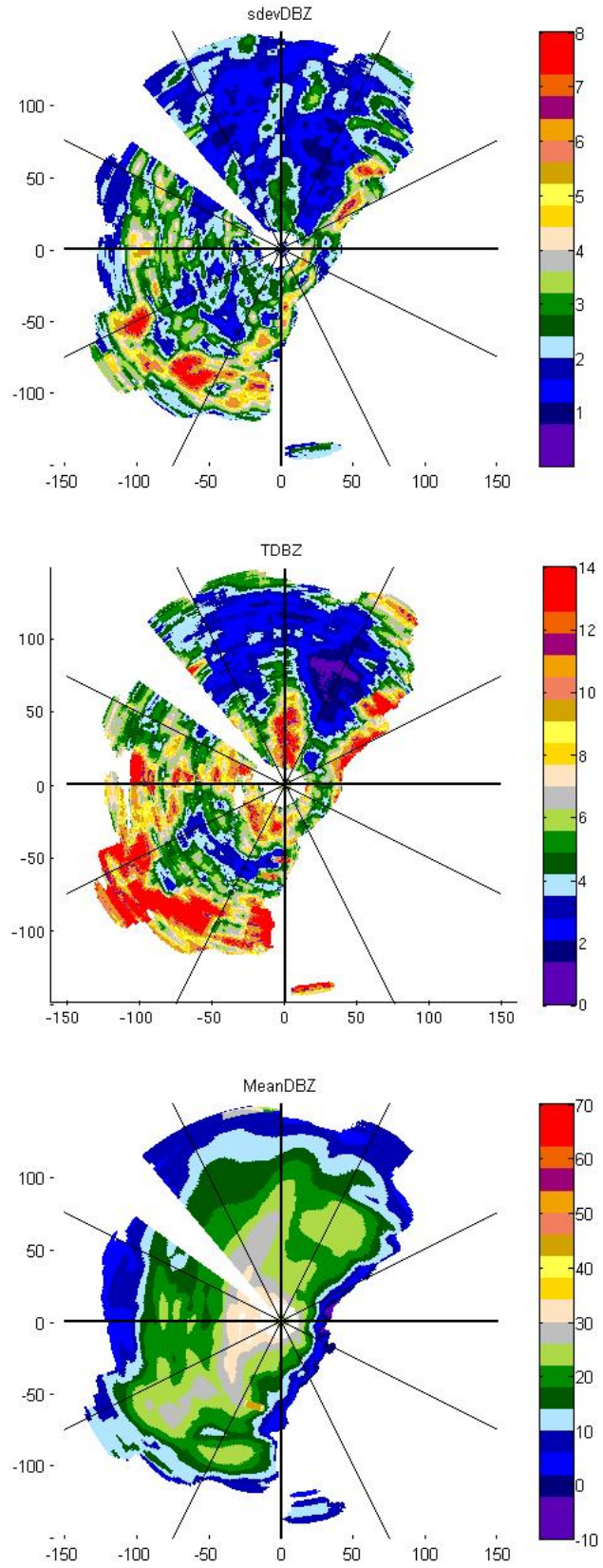
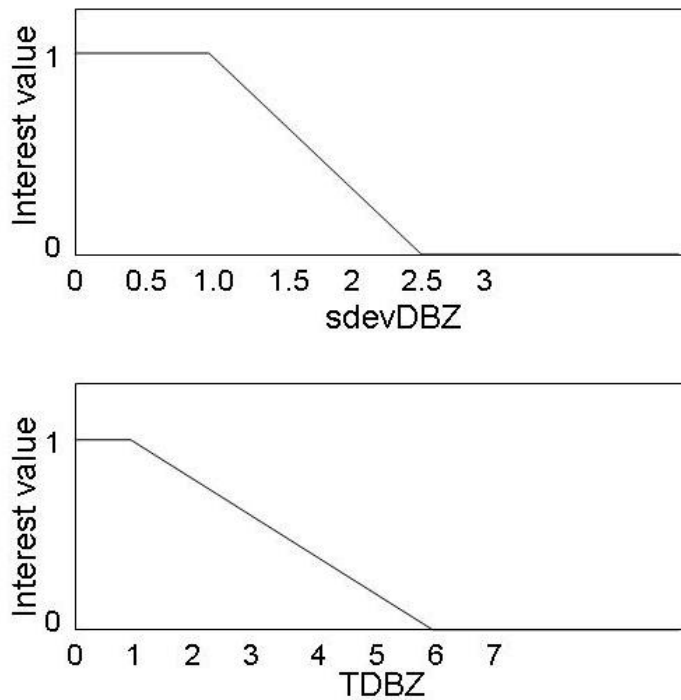Figure 41: *Local standard deviation (top), texture (middle), and mean (bottom) of dBZ.*

Figure 42: *Membership functions for sdevDBZ and TDBZ.*

sdev(sdevDBZ), and median(sdevDBZ) are defined by Fig. 14a, c and d, respectively, in Ikeda et al (2009). The membership functions used for sdevDBZ and TDBZ are shown in Fig. 42. The next step in the fuzzy logic process is to multiply the interest values by weights. Generally speaking the weights can be static or dependent on the input. Currently we are using a weight of 1 for each feature-field.

Figure 43 shows the interest values at an elevation angle of $1.53°$ resulting from the application of the membership functions for MeanDBZ (top panel), sdevDBZ (middle panel), and TDBZ (bottom panel). The interest field for MeanDBZ is 0 for nearly all of the domain, while the interest for TDBZ and sdevDBZ show maxima in the regions to the north and south of CHILL corresponding to the lowest values of TDBZ and sdevDBZ. Figure 44 shows the interest values of sdev(sdevDBZ) and median(sdevDBZ), which indicate the degree to which each layer (0.4 km) resemble the signature of freezing drizzle as defined by Ikeda et al. (2009). Both sdev(sdevDBZ) and median(sdevDBZ) show interest values of 1 at ranges closer than about 80 km.

The final step in this initial, simple fuzzy logic algorithm developed here is to compute the sum of the weighted interest values and normalize by the sum of the weights. The result is a combined output from 0 to 1 with values below 0.5 indicating low probability of icing and values close to 1.0 indicating a higher probability of icing conditions. Figure 45 shows the combined output at elevation angles of $1.53°$ (top) and $2.71°$ (bottom) for the present case. The results show regions of icing potential centered at about 50 km for both scans. This is again consistent with the pilot reports. There is high icing potential identified at the farthest ranges at $1.53°$ that is not present at $2.71°$ This discrepancy should be investigated in the future.
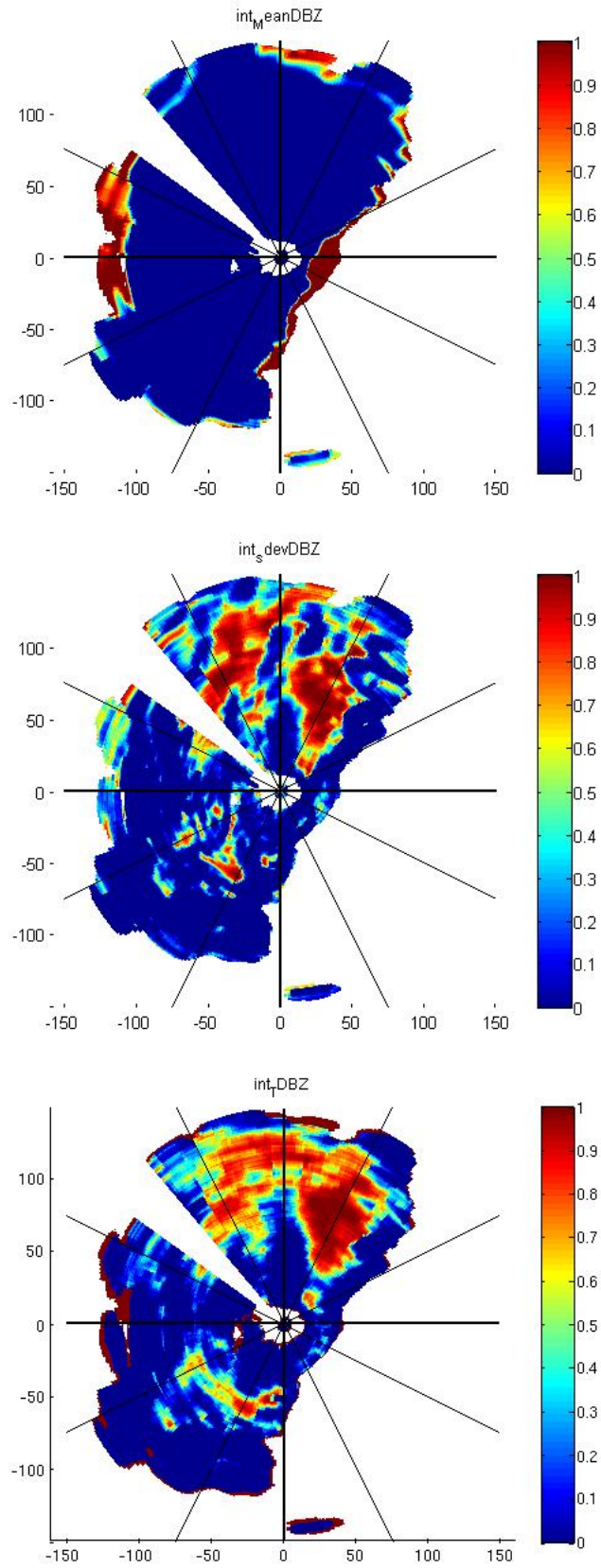
Figure 43: *Interest values of the local standard deviation (top), texture (middle), and mean (bottom) of dBZ.*
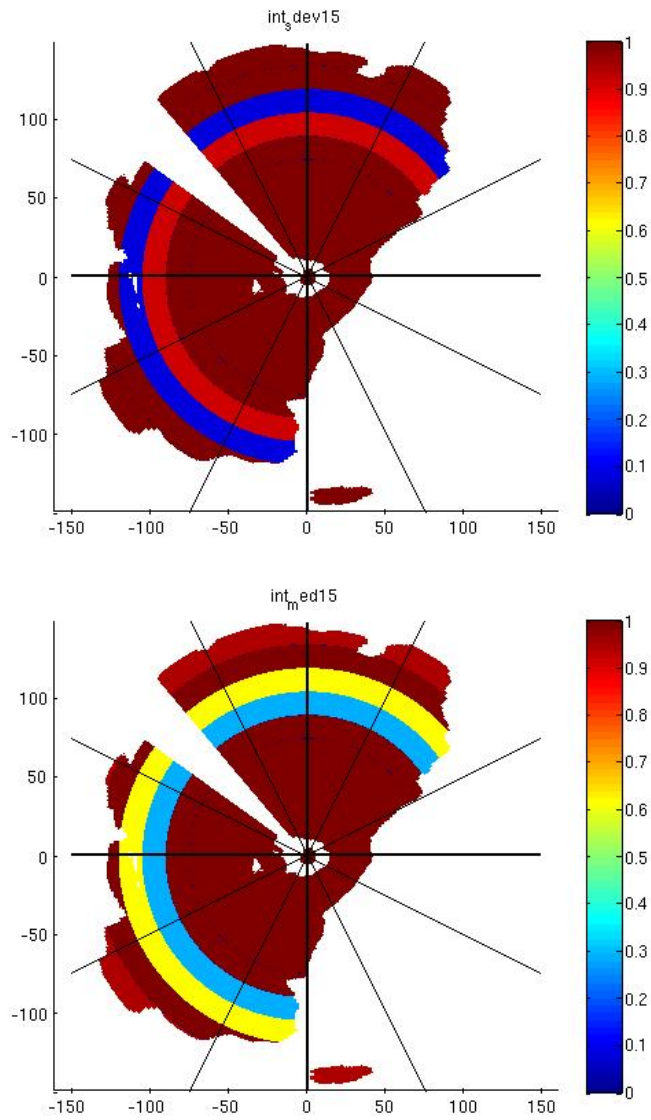
47

Figure 44: *Interest values of the standard deviation (top), and median (bottom) of the local standard deviation of dBZ computed over 15-km width bands.*
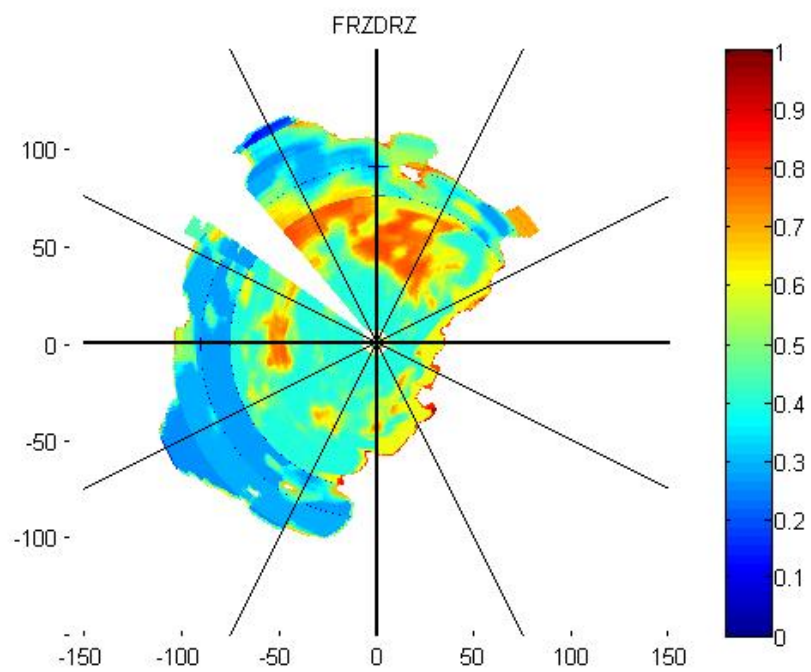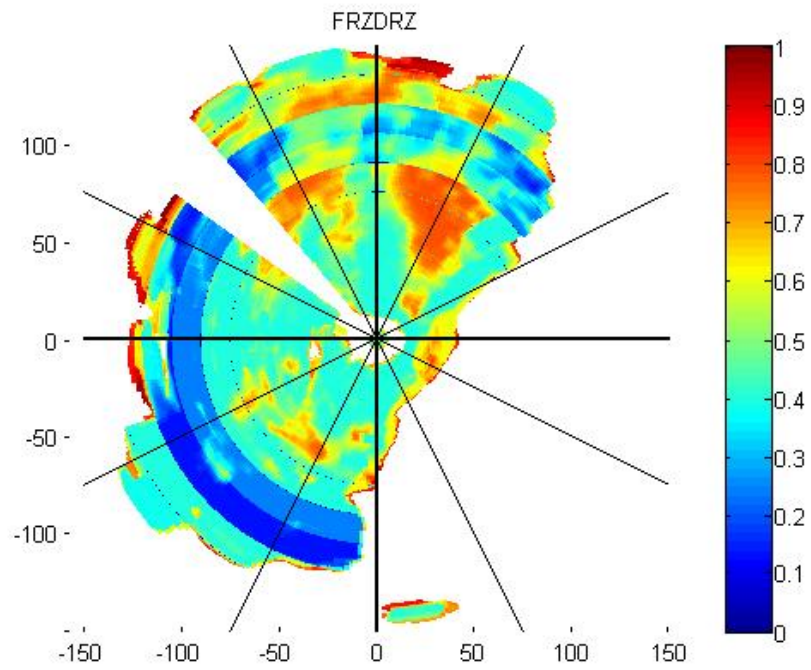
Figure 45: *Output of the fuzzy logic algorithm to SLD indicating the relative likelihood of icing conditions due to SLD.*

c *Identifying Mixed-Phase*

Plummer et al. (2010) document the dual-polarimetric signatures of mixed-phase icing conditions and ice-only conditions. They found that although the measurements at individual radar range gates have significant overlap, there are distinguishable differences in the characteristics of the overall populations of mixed-phase and ice-only. These distinguishing characteristics include the mean and standard deviation of Z_{dr} and K_{dp} computed over a local area. Plummer et al. (2010), found the mean of the Z_{dr} in mixed-phase conditions to be 0.01 dB compared to 0.20 for ice-only. For K_{dp} the mixed-phase conditions had a mean value of 0.01°/km compared to 0.06°/km in ice-only. Plummer et al. (2010) also show that the distributions of both Z_{dr} and K_{dp} have larger standard deviations for the ice-only population.

Figure 46 shows a plot at 1.53° elevation of the mean Z_{dr} and K_{dp} computed over the same local area defined by Ikeda et al. (2009). Figure 47 shows a plot at 1.53° elevation of the standard deviation of Z_{dr} and K_{dp} computed again over the same local area defined by Ikeda et al. (2009). The lower values in Figs. 46 and 47 indicate a higher likelihood of mixed-phase icing conditions.

Based on the results of Plummer et al. (2010), membership functions were designed and applied to the data to produce interest values and are shown in Fig. 48. Fig. 49 shows the interest values for the mean of Z_{dr} (top) and K_{dp} (bottom) and Fig. 50 shows the interest values for the standard deviation of Z_{dr} (top) and K_{dp} (bottom).

Next the four interest value fields were combined into a weighted sum and normalized to obtain an output from 0 to 1 with values below 0.5 indicating low probability of icing and values close to 1.0 indicating a higher probability of icing conditions. Figure 51 shows the mixed-phase identification output based on Plummer et al. (2010) for elevation angles of 1.53° (top) and 2.71° (bottom). The mixed-phase identification from this simple algorithm indicates a high possibility of icing in similar regions as the SLD results in Section b. These results are generally consistent with the pilot reports of icing at heights between about 1.3 to 3.1 km above the CHILL radar.
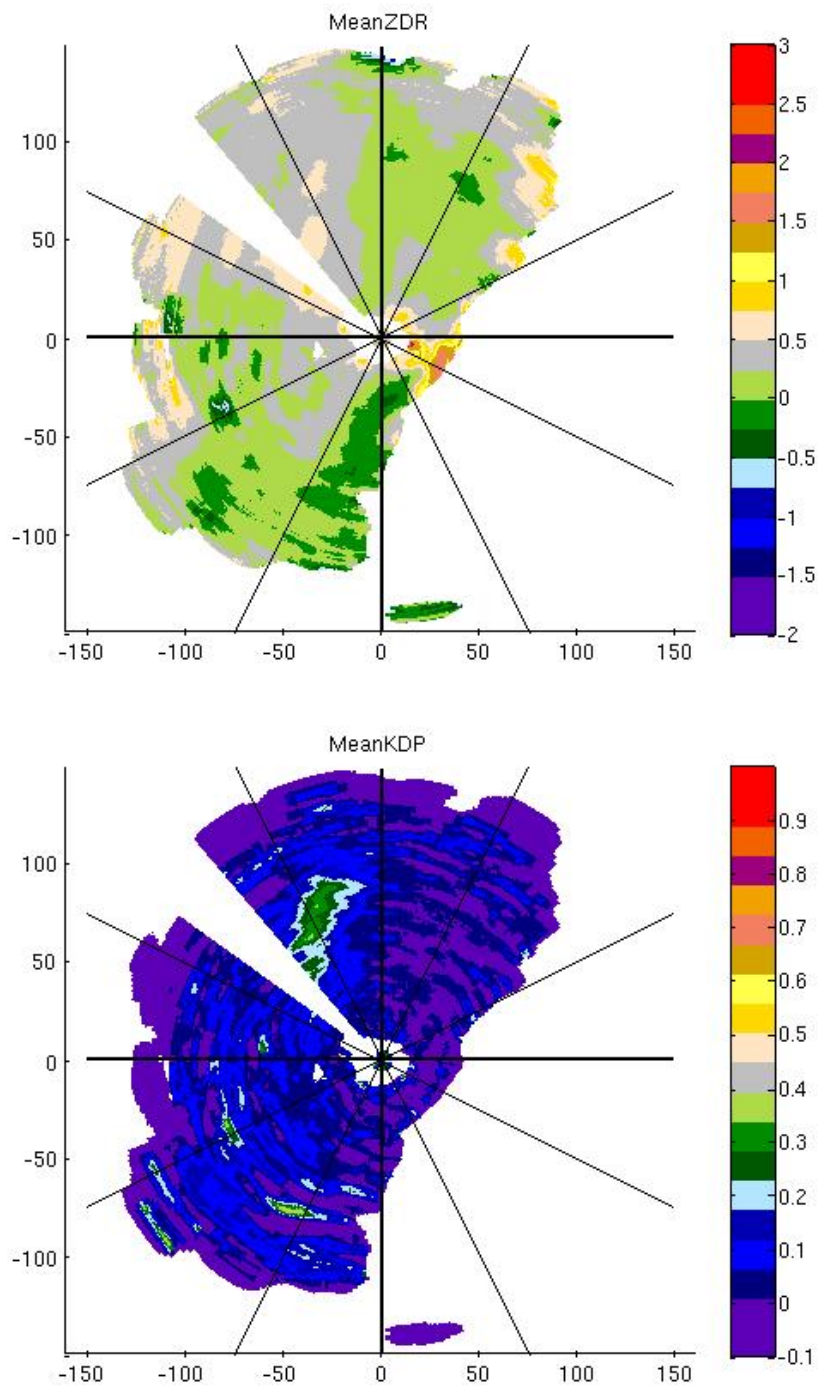
Figure 46: *Plots of local mean of Z_{dr} (top) and K_{dp} (bottom) at 1.53° elevation.*
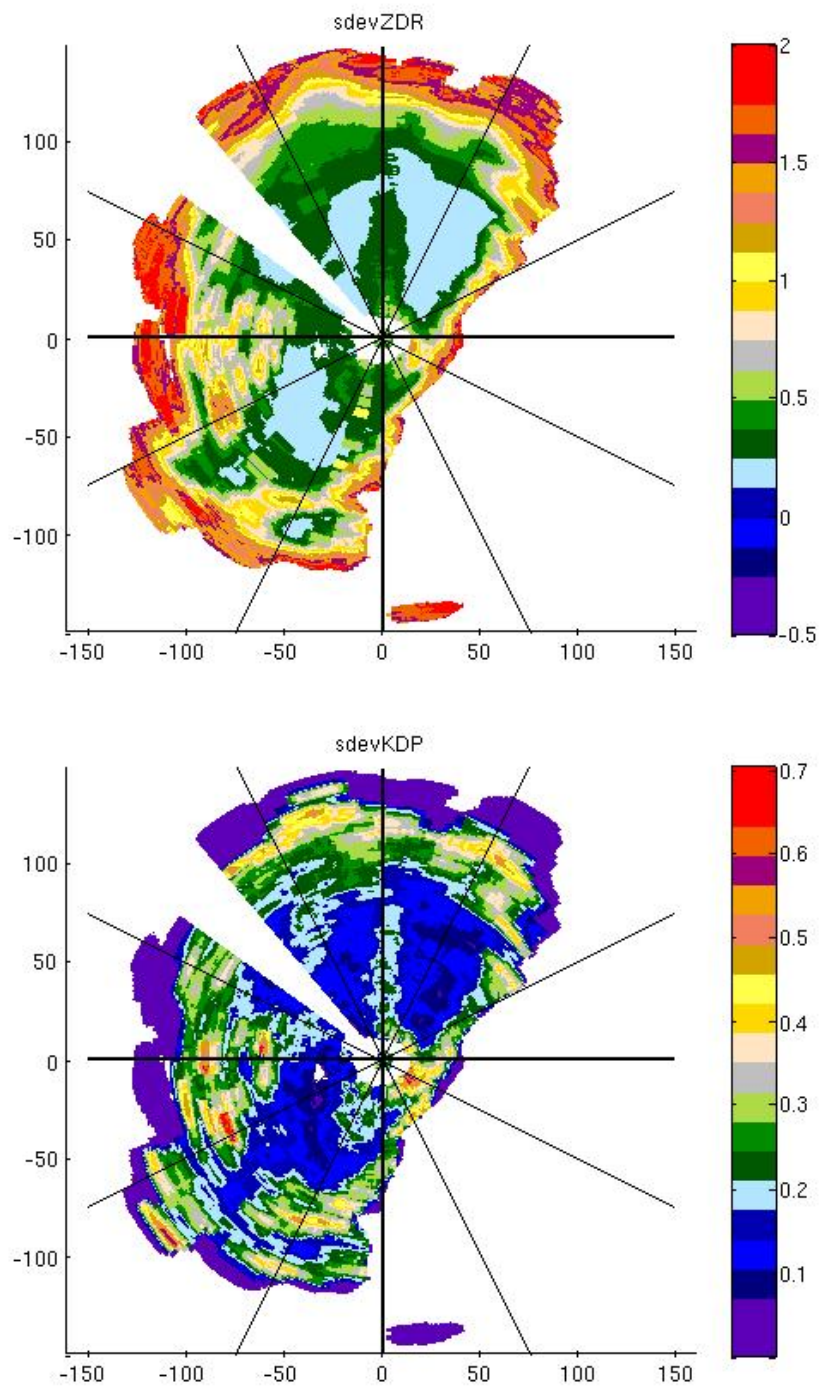
Figure 47: *Plots of local standard deviations of Z_{dr} (top) and K_{dp} (bottom) at 1.53° elevation.*
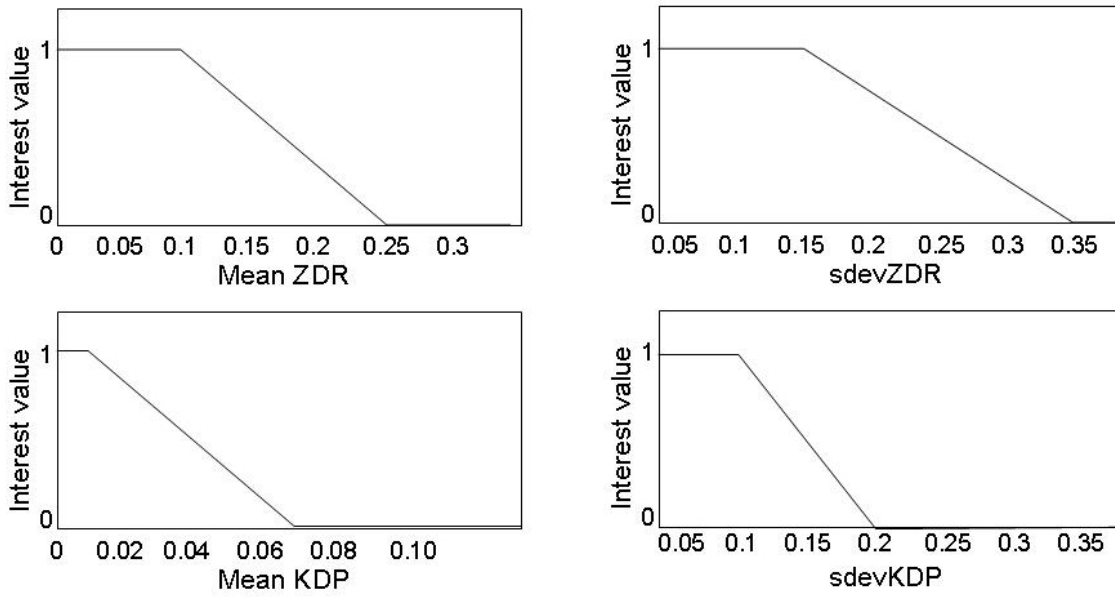
Figure 48: *Membership functions for the mean of Z_{dr}, mean of K_{dp}, sdevZDR and sdevKDP.*
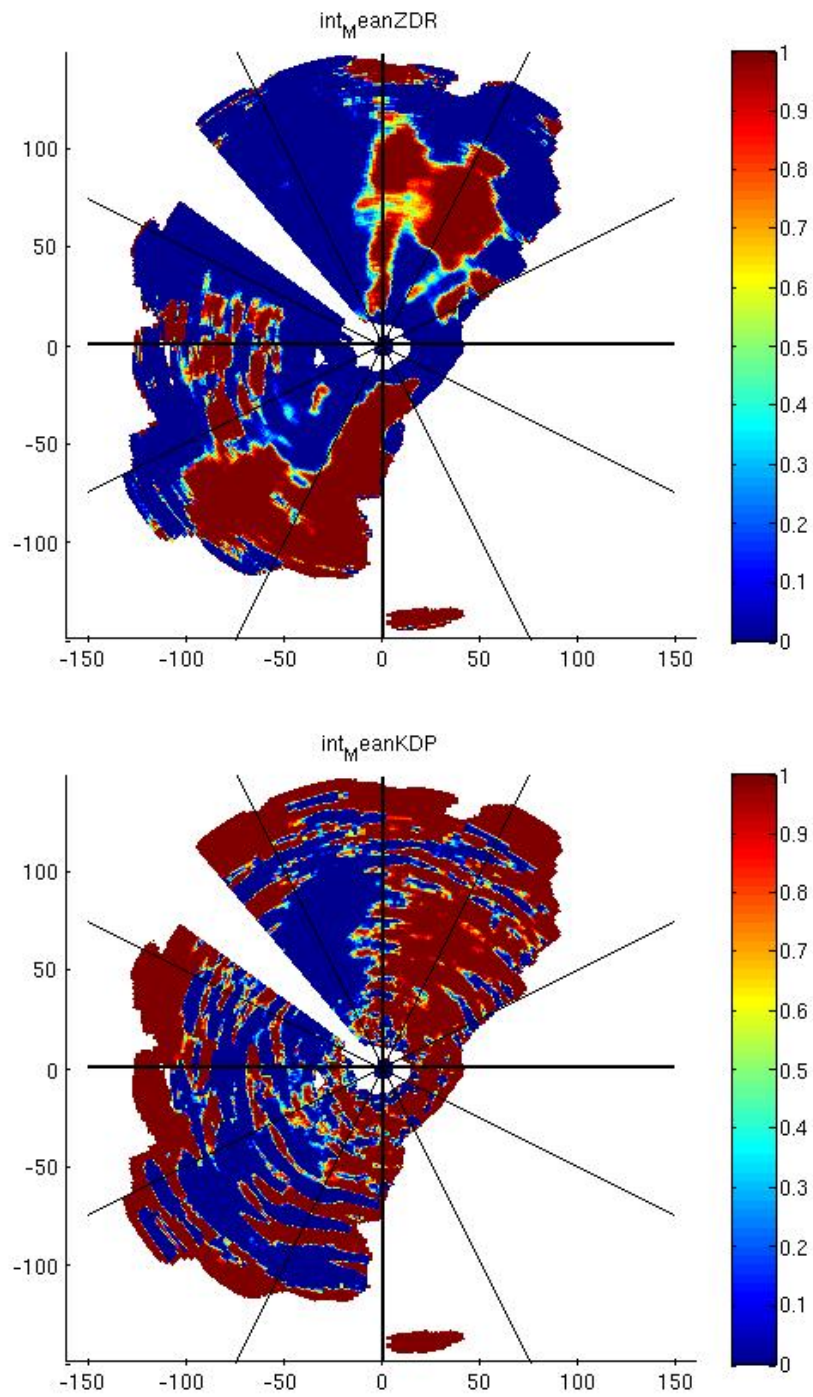
Figure 49: *Plots of the interest values for the local mean of Z_{dr} (top) and KDP (bottom) at 1.53° elevation.*
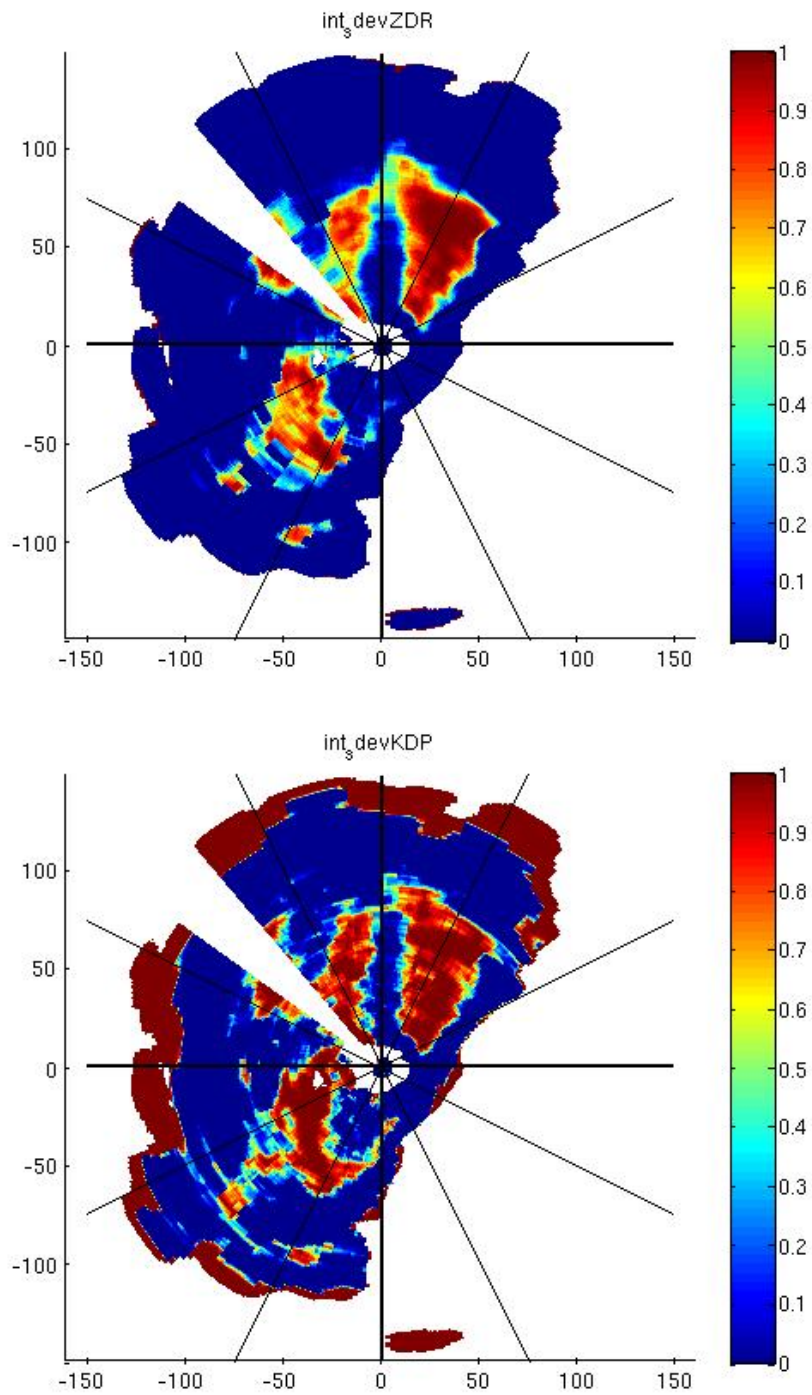
Figure 50: *Plots of the interest values for the local standard deviations of ZDR (top) and K_{dp} (bottom) at 1.53° elevation.*
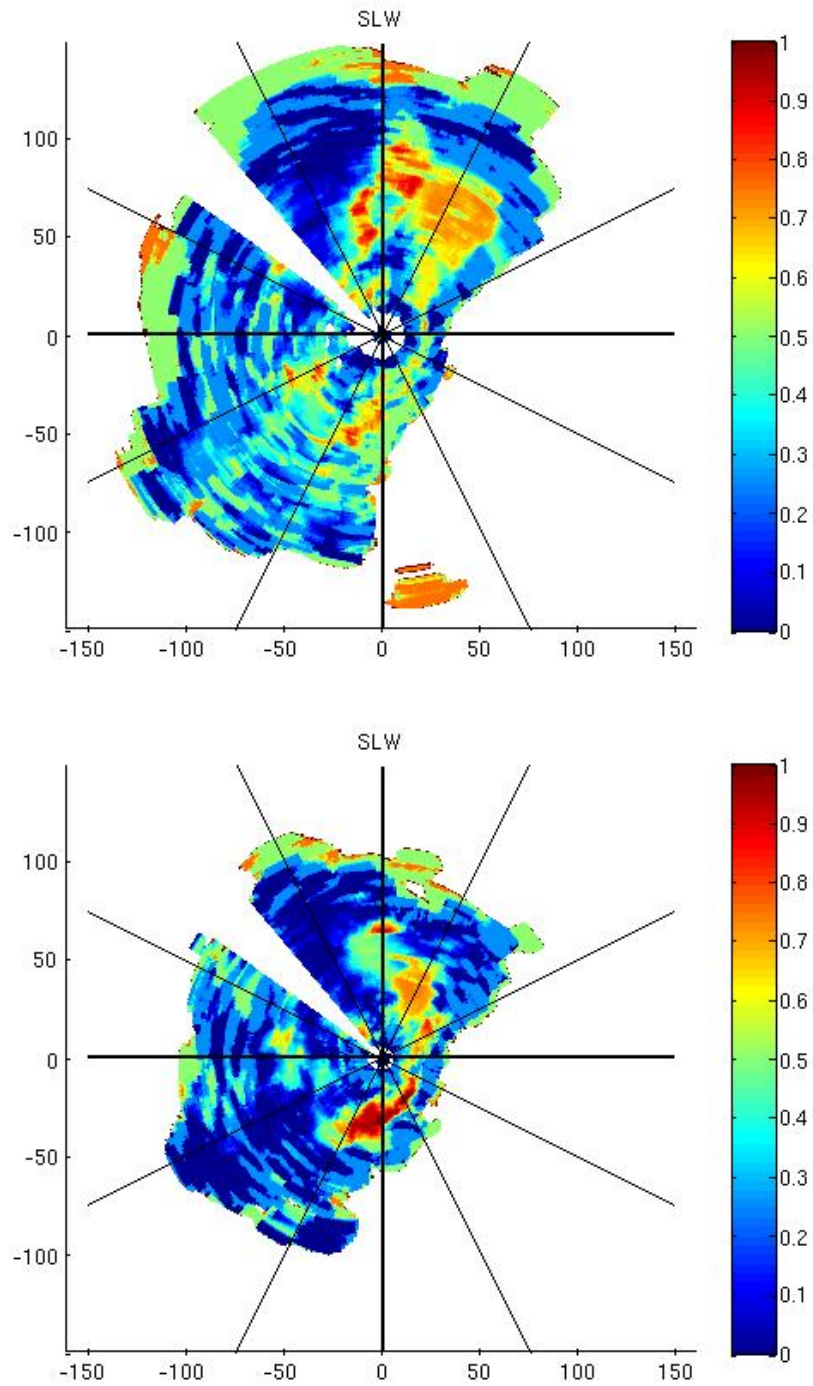
Figure 51: *Plots of the combined output for mixed-phase icing conditions at 1.53° (top) and 2.71° (bottom) elevation angles.*

10 Summary and Discussion

In this initial study, the results of two publications describing the radar signatures of two different types of icing conditions, namely supercooled drops and mixed-phase, were utilized to examine possibility of radar icing detection. The feature-fields described by Ikeda et al. (2009) to identify freezing drizzle were extended in order to test SLD detection above the ground. Also, dual-polarization feature-fields for detection of mixed-phase were computed following Plummer et al. (2010). It was found that the feature-fields described by Ikeda et al. (2009) and Plummer et al. (2010) both indicated an increased likelihood of icing at heights consistent with pilot reports near the time of the radar observations. Furthermore, the feature-fields for supercooled liquid and mixed-phase were combined in separate, simple fuzzy logic identification algorithms and produced results that indicated icing in similar regions, both qualitatively consistent with pilot reports.

The fact that the two algorithms searching for two different types of icing conditions (SLD and mixed-phase) yield similar results may at first be confusing. It can be explained because the radar signatures described by Ikeda et al. (2009) and Plummer et al. (2010) have similar characteristics, i.e., low variance of radar variables. For example, the SLD detection is looking for widespread spherical drops that will result in low variation in dBZ while the mixed-phase detection is looking for spherical riming particles that will result in low variation of Z_{dr} and K_{dp}. Therefore it is not surprising that the regions detected by the two algorithms are similar. In the case presented here, the icing conditions were most likely marked by mixed-phase conditions evidenced by the high dBZ values (recall the interest value of the mean dBZ field for SLD was 0 through most of the domain). In the future we will explore to what extent these two sets of feature fields and fuzzy logic algorithms can be combined.

The initial results are encouraging and may indicate that dual-polarimetric radar measurements have value in detecting icing conditions. However, more case studies using data with icing verification are required to validate the radar signatures (feature-fields) and fuzzy logic algorithms. Analysis of known icing cases and known non-icing cases is required to estimate the performance of the feature fields and algorithms.

Also, there are numerous ways to combine the radar feature-fields shown in this report and many experiments should be performed to maximize icing detection and minimize false alarms. Further analysis should be performed with the goal of optimizing the membership functions and weights. New feature-fields also should be investigated that could lead to increased skill. The algorithm needs to incorporate the detection of icing arising for different microphysical processes that may have different radar signatures. Performance of targeted field measurements including high quality dual-polarization radar measurements in combination with icing ground truth is highly desirable to this investigation.

The combined resources of the CSU-CHILL and NCAR S-PolKa radars (known as the Front Range Observational Testbed, FRONT) provides an excellent opportunity for field measurements that would be invaluable to this study. It is planned to collect more data with S-PolKa and CHILL this upcoming Fall and Winter seasons. Comparison to pilot reports from the various Front Range airports can be used as verification. There is a possibility of obtaining the NASA/GLEN NIRSS system to support S-PolKa and CSU-CHILL measurements.

References

Berstein, B., F. McDonough, T. R. M.K. Politovich, B.G. Brown, D. Miller, C. Wolff, and G. Cunning, 2005: Current Icing Potential: Algorithm description and comparison to aircraft obsevations. *J. Appl. Meteor.*, **44**, 969–986.

Brandes, E. A. and K. Ikeda, 2004: Freezing-level estimation with polarimetric radar. *J. Appl. Meteor.*, **43**, 1541–1553.

Fabry, F. and I. Zawadski, 1995: Long-term radar observations of the melting layer of precipitation and their interpretation. *J. Atmos. Sci.*, **52**, 838–851.

Ikeda, K., R. M. Rasmussen, E. A. Brandes, and F. McDonough, 2009: Freezing drizzle detection with WSR-88D radars. *J. Appl. Meteor. Climat.*, **48**, 41–60.

Plummer, D. M., S. Göke, R. M. Rauber, and L. D. Girolamo, 2010: Discrimination of Mixed- versus Ice-Phase Clouds Using Dual-Polarization Radar with Application to Detection of Aircraft Icing Regions. *J. Appl. Meteor. Climat.*, **49**, 920–936.

Rinehart, R., 2004: *Radar for meteorologists*. Rinehart Publications, Columbia, MO, 482 pp.

Vivekanandan, J., D. Zrnić, S. M. Ellis, R. Oye, A. Ryzhkov, and J. Straka, 1999: Cloud microphysics retrieval using S-band dual-polarization radar measurements. *Bull. Amer. Meteor. Soc.*, **80**, 381–388.